

# Semi-analytic construction of global transfers between quasi-periodic orbits in the spatial R3BP

Amadeu Delshams<sup>a</sup>, Marian Gidea<sup>b</sup>, Pablo Roldan<sup>c,\*</sup>

<sup>a</sup>*Laboratory of Geometry and Dynamic Systems and IMTech, Universitat Politècnica de Catalunya (UPC) and Centre for Mathematical Research (CRM), Barcelona, Spain*

<sup>b</sup>*Department of Mathematical Sciences, Yeshiva University, New York, 10016, NY, USA*

<sup>c</sup>*Departament de Matemàtiques, Universitat Politècnica de Catalunya (UPC), Barcelona, 08028, Spain*

---

## Abstract

Consider the spatial restricted three-body problem, as a model for the motion of a spacecraft relative to the Sun-Earth system. We focus on the dynamics near the equilibrium point  $L_1$ , located between the Sun and the Earth. We show that we can transfer the spacecraft from a quasi-periodic orbit that is nearly planar relative to the ecliptic to a quasi-periodic orbit that has large out-of-plane amplitude, at zero energy cost. (In fact, the final orbit has the maximum out-of-plane amplitude that can be obtained through the particular mechanism that we consider. Moreover, the transfer can be made through any prescribed sequence of quasi-periodic orbits in between).

Our transfer mechanism is based on selecting trajectories homoclinic to a normally hyperbolic invariant manifold (NHIM) near  $L_1$ , and then gluing them together. We provide several explicit constructions of such transfers, and also develop an algorithm to design trajectories that achieve the *shortest transfer time* for this particular mechanism.

The change in the out-of-plane amplitude along a homoclinic trajectory can be described via the scattering map. We develop a new tool, the ‘Standard Scattering Map’ (SSM), which is a series representation of the exact scattering map. We use the SSM to obtain a complete description of the dynamics along homoclinic trajectories. The SSM can be used in many other situations, from Arnold diffusion problems to transport phenomena in applications.

---

\*Corresponding author

*Email address:* Pablo.Roldan@upc.edu (Pablo Roldan)

*Keywords:* Three-body problem, Transfer orbit, Quasi-periodic orbit, Scattering map, Arnold diffusion

---

## 1. Introduction

In this paper, we consider the spatial circular restricted three-body problem (RTBP for short), as a model for the motion of spacecraft relative to the Sun-Earth system. We focus on the dynamics near the equilibrium point  $L_1$  located between the Sun and the Earth. We show that we can transfer the spacecraft, at zero energy cost, from a quasi-periodic orbit that is nearly planar relative to the ecliptic to a quasi-periodic orbit of large out-of-plane amplitude. That is, we can achieve a change in the out-of-plane amplitude of the orbit of the spacecraft simply by choosing suitable initial conditions and letting the gravitational fields of the Sun and the Earth drive the motion. Moreover, we provide several explicit constructions of such trajectories, and also develop an algorithm to design trajectories that achieve the shortest transfer time. Our algorithm is flexible and can be applied to other systems besides Sun-Earth.

For illustration, Figure 1 shows the initial and final segments (in blue and green, respectively) of the fastest transfer trajectory between one quasi-periodic orbit with small vertical amplitude, and another with large vertical amplitude.

The model that we consider is a 3-degrees of freedom Hamiltonian system. We construct trajectories that follow closely geometric structures that organize the dynamics. The main geometric object near  $L_1$  is a center manifold on which the dynamics is nearly integrable. More precisely, in a neighborhood of  $L_1$  the Hamiltonian can be approximated by a high-order Birkhoff normal form, which is an integrable Hamiltonian. In terms of the normal form, the center manifold is represented by a 4-sphere, which is foliated by a family of 2-dimensional invariant tori. The sphere can be parametrized by a system of symplectic coordinates consisting of two action variables  $(I_p, I_v)$  and two angle variables  $(\phi_p, \phi_v)$ , with each torus corresponding to a pair of fixed values of the two actions. The action  $I_p$  describes the horizontal amplitude (relative to the ecliptic) of an orbit lying on a 2-dimensional torus, and  $I_v$  describes the vertical amplitude. Restricting to an energy level close to that of  $L_1$  amounts to fixing the action variable  $I_p$ . This yields a 3-dimensional sphere which is filled with 2-dimensional tori. Each torus is given by a fixed value of

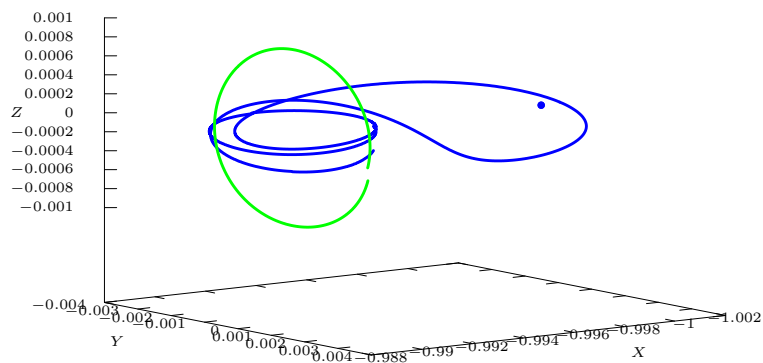


Figure 1: Initial segment (blue) and final segment (green) of the fastest transfer trajectory between a quasi-periodic orbit with small vertical amplitude (small  $Z$ -oscillation), and another with large vertical amplitude ( $Z$ -oscillation of amplitude 0.001, roughly 150000 km). The complete trajectory (not shown here) is very complicated, and goes through many homoclinic jumps. This trajectory is computed in Section 11.2. (See also Figures 22 and 23).

the remaining action variable  $I_v$ . A change in  $I_v$  corresponds to a change in the out-of-plane amplitude of the orbit. Since the tori are invariant, by using only the ‘inner flow’ restricted to the 3-dimensional sphere, the out-of-plane amplitude of orbits remains constant. In order to change the out-of-plane amplitude, we need to use the ‘outer dynamics’, described below.

The 3-dimensional sphere is a normally hyperbolic invariant manifold (NHIM), and has stable and unstable manifolds which go around the Earth and intersect transversally along trajectories homoclinic to the NHIM. By taking repeated excursions along the homoclinic trajectories, we show that it is possible to achieve large changes in the out-of-plane amplitude of orbits. However, if we would pick at random which homoclinic trajectories to follow, sometimes we will obtain a growth in the out-of-plane amplitude, and other times we will obtain a decay. In general, one expects that the values of  $I_v$  will follow a stochastic process, e.g., a Brownian motion with drift [1, 2]. To consistently achieve a growth in the out-of-plane amplitude, we need to carefully select which homoclinic trajectories to follow.

The tool that allows us to systematically select suitable homoclinics at each step is the *scattering map*. This is a map defined on the NHIM, which relates the past asymptotic of a homoclinic point to its future asymptotic. The scattering map was introduced in [3, 4, 5] in the study of Arnold diffusion. When restricted to a suitable 2-dimensional Poincaré section, the scattering map turns out to be symplectic [6, 7]. An additional advantage that we exploit in our model is that we obtain two scattering maps, which give us more options in the selection of suitable homoclinics. In general, Hamiltonian systems similar to the one we consider here exhibit multiple homoclinics and associated scattering maps.

In perturbative problems, the scattering map can be computed analytically via perturbation theory [6]. However, the problem that we consider is not perturbative. For such problems, the only available methods up to now to compute the scattering map have been numerical ones [8, 9]. Yet, the purely numerical approach is computational intensive and offers little insights into the geometric structures determined by the scattering map.

The highlight of this paper is that we provide an analytical approximation of the scattering map for the spatial circular RTBP. We describe the scattering map via a generating function depending on old and new variables. Then we approximate the generating function using a Fourier-Taylor expansion. As it turns out, the numerical computation of the scattering map at a few points can be used to compute the coefficients of the Fourier-Taylor

expansion, up to some suitable order, and thus to obtain an analytical formula for the generating function, up to some small error. The outcome of this approximation is referred to as the *Standard Scattering Map* (SSM). It is given explicitly as a perturbation of an integrable twist map. As such, the phase space of the scattering map is organized by KAM tori, elliptic islands, hyperbolic periodic orbits and their stable and unstable manifolds, and resonant zones. See Figure 16. The rich geometric structure unveiled by the analytical approximation of the scattering map was not available through previous approaches. Similar computations of the generating function of the scattering map and of its phase space were obtained purely analytically in uncoupled pendulum-rotor systems subject to small perturbations of a special type [10, 11]. However, as the unperturbed pendulum-rotor systems considered in these papers are uncoupled, the phase shift phenomenon [12] does not take place, and the unperturbed scattering maps are just the identity. In particular, they are not twist maps, which makes the dynamics different from those considered in this paper.

The main application of the Standard Scattering Map is that it offers an explicit method to find pseudo-orbits of the iterated function system consisting of the scattering map and the inner map (induced by the inner flow on the Poincaré section), along which the orbit out-of-plane amplitude  $I_v$  grows consistently. The method is versatile, in the sense that one can choose the starting and ending points of such pseudo-orbits. As mentioned earlier, in this paper we compute two scattering maps, and we compare them in terms of the fastest trajectory to achieve the desired change in out-of-plane amplitude.

It is important to note that the pseudo-orbits of the scattering maps are not equivalent to true trajectories of the system. Rather, we can approximate a segment of a homoclinic trajectory by a concatenation of a finite orbit of the inner dynamics, followed by an application of a scattering map, followed by another finite orbit of the inner dynamics. We refer to the map that assigns to the starting point of this concatenation of orbits its ending point, as the *transition map*. The transition map is a map on the NHIM, and each application of the transition map corresponds to a segment of a homoclinic orbit to the NHIM. Since we have constructed two scattering maps, we have two corresponding transition maps. To obtain approximate trajectories that change the orbital out-of-plane amplitude, we consider the iterated function system consisting of the two transition maps and the inner map, and we search for optimal trajectories.

Towards this goal, we leverage the classic Dijkstra algorithm for finding shortest paths in a graph. A surprising finding is that for an optimal pseudo-orbit of the iterated function system, rather than always selecting a transition map that grows  $I_v$ , sometimes we must select a transition map that decreases  $I_v$ , in order to arrive to a place where the next application of a transition map yields a large increase in  $I_v$ . Another surprising finding is that an optimal pseudo-orbit involves very few applications of the inner map.

Our construction described so far is based on approximating the Hamiltonian near  $L_1$  by a Birkhoff normal form. Since the approximation is quite accurate, the true dynamics associated to the original Hamiltonian follow closely the normal form dynamics. In particular, the trajectories of the true inner dynamics stay close to invariant tori, and the scattering map for the true dynamics is close to the scattering map derived from the normal form approximation. This implies that there exist diffusing trajectories – that change the orbital out-of-plane amplitude by a significant amount – for the original Hamiltonian system.

Our results are related to the Arnold diffusion problem for Hamiltonian systems, claiming that integrable Hamiltonian systems subjected to small perturbations of generic type have ‘diffusing orbits’ along which the action variable changes by an amount independent of the smallness of the perturbation [13]. Arnold illustrated this phenomenon for an uncoupled pendulum-rotor system subject to small perturbations of special type. To prove the existence of diffusing orbits, he constructed transition chains of tori, which are sequences of invariant tori with consecutive heteroclinic connections between consecutive tori. Arnold conjectured: “I believe that this mechanism of instability is applicable to the general case (for example, to the problem of three bodies)”. This conjecture has witnessed significant progress in recent years, including [14, 15, 3, 16, 17, 18, 4, 5, 19, 20, 21, 22, 23, 24, 25, 26, 27, 28, 29, 30, 31]. Some of the progress has been geared towards proving Arnold diffusion in concrete models, under explicit, verifiable conditions on the perturbation. This direction opened up the possibility of implementing Arnold’s mechanism of diffusion in applications, such as to Celestial Mechanics. Notably, some papers, including [32, 33, 34], succeeded in providing analytical proofs of Arnold Diffusion in some models of the three- and four-body problem. These papers rely on perturbative methods, and therefore they need to assume that certain parameters (such as ratios of the masses of the bodies, or ratios of the semi-major axes of the orbits) are very small, in fact much smaller than those observed in solar systems. Another line of ar-

guments combine analytical methods with numerical computation (including computer assisted proofs) to show Arnold diffusion in models with realistic parameters, see, e.g. [35, 1, 36].

Our paper follows this latter approach. To construct orbits that change their out-of-plane amplitude over time we implement Arnold’s mechanism of transition tori via analytical tools and numerical methods. We use the scattering maps described above to construct heteroclinic chains of invariant tori that lie inside the NHIM, such that the action  $I_v$  changes significantly along these chains. Since the model that we consider is not perturbative, we cannot say that this change is by an amount independent of some smallness parameter, but we can argue that the change is as large as the geometric mechanism on hand allows. Specifically, we show that the action changes over the whole domain of the scattering map, which covers about 70% of the region where primary homoclinics exist. (See Section 3.3).

The construction in this paper can be potentially adapted to astrodynamics applications. Sometimes, a satellite (which typically carries little fuel) ends up on a wrong orbit, and one tries to correct the orbit by exploiting the gravity of Earth, Sun, Moon as much as possible, and firing the satellites’ thrusters as little as possible; see, e. g., [37]. While our methodology to change the out-of-plane amplitude of a satellite orbit may be too slow from a practical point of view, by combining zero-cost geometric routes with small thrusts, one may be able to design useful trajectories. Moreover, our methodology can be applied to build transfers involving two or more NHIMs connected by heteroclinic orbits, e.g. the NHIM around  $L_1$  and that around  $L_2$  [12, 38].

## 2. Setup

### 2.1. The Spatial Circular RTBP

We consider the spatial circular RTBP as a model for the motion of a satellite under the gravitational influence of the Sun and the Earth. In this model, two heavy bodies (referred to as primaries) move in the same plane along circular orbits about their common center of mass, while a third, infinitesimal body (referred to as secondary) moves in space under the gravitational influence of the heavy bodies, without affecting their orbits. It is convenient to use a co-rotating frame  $XYZ$  whose origin  $O$  is set at the center of mass of the system, such that the orbits of the primaries lie in the  $XY$ -plane, and the out-of-plane component of the motion of the secondary

is given by the  $Z$ -coordinate. The units are normalized so that the masses of the primaries are  $\mu_1$  and  $\mu_2$ , with  $\mu_1 + \mu_2 = 1$ , the distance between the primaries is 1, the period of the motion of the primaries is  $2\pi$ , and the gravitational constant is  $G = 1$ . Denoting the smaller mass by  $\mu = \mu_2$  and the larger one by  $1 - \mu = \mu_1$ , the larger body is located on the  $X$ -axis to the right of  $O$  at  $P_1 = (\mu, 0, 0)$ , and the smaller body is located on the  $X$ -axis to the left of  $O$  at  $P_2 = (\mu - 1, 0, 0)$  (see Figure 2).

In the case of the Sun-Earth system  $\mu = 3.040423398444176 \times 10^{-6}$ .

The motion of the secondary relative to these coordinates is given by the autonomous system of equations:

$$\begin{aligned}\ddot{X} - 2\dot{Y} &= \Omega_X, \\ \ddot{Y} + 2\dot{X} &= \Omega_Y, \\ \ddot{Z} &= \Omega_Z,\end{aligned}\tag{1}$$

where the effective potential  $\Omega$  is given by

$$\Omega = \frac{1}{2}(X^2 + Y^2) + \frac{1 - \mu}{r_1} + \frac{\mu}{r_2},$$

with  $r_1, r_2$  representing the distances from the secondary to the larger and the smaller primary, respectively:

$$\begin{aligned}r_1 &= ((X - \mu)^2 + Y^2 + Z^2)^{1/2}, \\ r_2 &= ((X - \mu + 1)^2 + Y^2 + Z^2)^{1/2}.\end{aligned}$$

The phase space is 6-dimensional.

The system has an integral of motion (referred to as the Jacobi integral) given by:

$$C = 2\Omega - (\dot{X}^2 + \dot{Y}^2 + \dot{Z}^2).$$

Equivalently, the equations (1) can be described as a 3-degree-of-freedom, autonomous Hamiltonian system given by the Hamiltonian function:

$$H = \frac{1}{2}(P_X^2 + P_Y^2 + P_Z^2) + YP_X - XP_Y - \frac{1 - \mu}{r_1} - \frac{\mu}{r_2},\tag{2}$$

where  $X, Y, Z$  are the generalized coordinates,  $P_X = \dot{X} - Y$ ,  $P_Y = \dot{Y} + X$ ,  $P_Z = \dot{Z}$  are the generalized momenta, and the symplectic form is:

$$dP_X \wedge dX + dP_Y \wedge dY + dP_Z \wedge dZ.$$



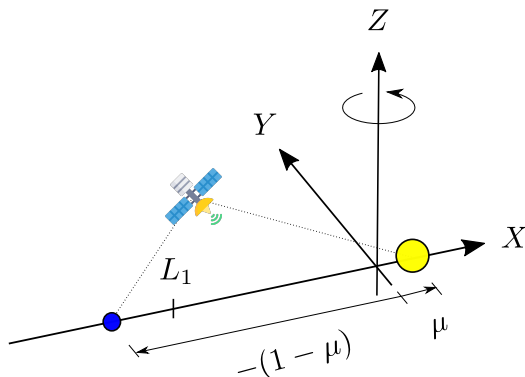


Figure 2: Schematic location of the Sun (in yellow), the Earth (in blue), and the equilibrium point  $L_1$ .

The Hamiltonian function and the Jacobi integral are equivalent integrals of motion, since

$$H = -\frac{C}{2}.$$

As the Hamiltonian (and, equivalently, the Jacobi integral) is preserved along the solutions of the system, each trajectory lies on a 5-dimensional energy manifold  $M_h$  corresponding to some energy level  $h$ , that is,

$$M_h = \{H(X, Y, Z, P_X, P_Y, P_Z) = h\},$$

or, equivalently, on the level surface of the Jacobi integral

$$M_h = \{C(X, Y, Z, \dot{X}, \dot{Y}, \dot{Z}) = c = -2h\}.$$

The system has 5 equilibrium points, denoted  $L_1, \dots, L_5$ . Here we adopt the convention that  $L_1$  is located between the primaries (see Figure 2). The equilibria  $L_1, L_2, L_3$  are of Saddle  $\times$  Center  $\times$  Center – linear stability type, and the equilibria  $L_4, L_5$  are of Center  $\times$  Center  $\times$  Center – linear stability type (provided that  $\mu$  is less than Routh’s critical value  $\mu_{cr}$ , which is always the case for the planets in our solar system).

A general reference for the RTBP is [39].

## 2.2. Local Dynamics around $L_1$

For the purpose of this paper, we focus on the dynamics near the equilibrium point  $L_1$  (a similar analysis can be performed near  $L_2$  and  $L_3$ ). The

quadratic part  $H_2$  of the Hamiltonian  $H$  given in (2), can be written, via a symplectic coordinate change

$$(P_X, P_Y, P_Z, X, Y, Z) \mapsto (y_1, y_2, y_3, x_1, x_2, x_3),$$

as

$$H_2 = \nu_h x_1 y_1 + \frac{\nu_p}{2}(x_2^2 + y_2^2) + \frac{\nu_v}{2}(x_3^2 + y_3^2),$$

where

$$\pm\nu_h, \pm i\nu_p, \pm i\nu_v, \text{ with } \nu_h, \nu_p, \nu_v \text{ real and positive,}$$

are the eigenvalues of the linearized system near  $L_1$ .

The coordinates  $x_1, y_1$  represent the hyperbolic directions of motion, while  $x_2, y_2, x_3, y_3$  represent the center directions. The quantities  $\nu_h, -\nu_h$  represent the exponential expansion and contraction rates in the hyperbolic directions, while  $\nu_p, \nu_v$  represent the frequencies of the planar and vertical components of the motion, respectively. By the Center Manifold Theorem (see e.g., [40]), there exists a 4-dimensional invariant center manifold that is tangent at  $L_1$  to the generalized eigenspace corresponding to  $\pm i\nu_p, \pm i\nu_v$ .

The Hamiltonian  $H$  can be expanded about  $L_1$ , via a symplectic coordinate change

$$(y_1, y_2, y_3, x_1, x_2, x_3) \mapsto (J_h, J_p, J_v, \phi_h, \phi_p, \phi_v),$$

as a Birkhoff normal form

$$\mathcal{H}^{(N)} = H_2 + \mathcal{Z}^{(N)} + \mathcal{R}^{(N)},$$

where  $H_2$  now denotes the quadratic part of  $H$  expressed in terms of the new variables,  $\mathcal{Z}^{(N)}$  is a polynomial of degree  $N$  that Poisson-commutes with  $H_2$ , and the remainder  $\mathcal{R}^{(N)}$  is small in a neighborhood of  $L_1$  (more precisely, of the order of the  $(N+1)$ -th power of the distance to  $L_1$ ). We refer to  $J_h, J_p, J_v$  as the action variables, and to  $\phi_h, \phi_p, \phi_v$  as the angle variables. The above power series expansion is not convergent in general, but only asymptotically convergent.

The truncated normal form depends only on the three actions  $J_h, J_p, J_v$ ,

$$\mathcal{H}_{\text{trunc}}^{(N)} = H_2 + \mathcal{Z}^{(N)} = \nu_h J_h + \nu_p J_p + \nu_v J_v + \mathcal{Z}^{(N)}(J_h, J_p, J_v),$$

which are integrals of motion for  $\mathcal{H}_{\text{trunc}}^{(N)}$ .

The variables  $(J_h, \phi_h)$  correspond to the hyperbolic component of the dynamics. In fact,  $J_h = x_1 y_1$ , where  $x_1, y_1$  are the unstable and stable coordinate, respectively. The center manifold around  $L_1$  corresponds to  $J_h = 0$ . The pair  $(J_p, \phi_p)$  corresponds to the *planar* component of the motion (thus the subscript  $p$ ), while  $(J_v, \phi_v)$  corresponds to the *vertical* component (thus the subscript  $v$ ).

A useful reference for the derivation of such a normal form is [41]. In [9], we performed the computation of this normal form for the spatial circular RTBP up to order  $N = 16$ . We will use this computation in this paper.

The truncated Birkhoff normal form  $\mathcal{H}_{\text{trunc}}^{(N)}$  represents an approximation of the original Hamiltonian  $H$ , and therefore the invariant objects for  $\mathcal{H}_{\text{trunc}}^{(N)}$  give approximations of the corresponding invariant objects of  $H$  (throughout the paper, we will provide error bounds on the approximations of specific objects). In particular, we consider the center manifold  $W^c(L_1)$  for the truncated Birkhoff normal  $H_{\text{trunc}}^{(N)}$ . This center manifold is completely foliated by 2-dimensional tori which can be parameterized using two action-angle pairs:

$$W^c(L_1) = \{(J_p, J_v, \phi_p, \phi_v)\}. \quad (3)$$

By comparison, the center manifold of  $L_1$  corresponding to the full Hamiltonian  $H$  contains a large family of 2-dimensional KAM invariant tori, with the gaps between tori of exponentially small size with respect to the actions  $J_p, J_v$  (see [42] for quantitative estimates). Therefore, the trajectories in the central manifold for  $H$  closely follow those for the truncated normal form approximation (3), for the times considered in this paper.

The order  $N = 16$  of the truncated normal ensures that the error between the true dynamics in the NHIM and the dynamics of the Birkhoff Normal Form is within machine precision. See Remark 4.

From now on, we only use the truncated Birkhoff normal form  $\mathcal{H}_{\text{trunc}}^{(N)}$  as an approximation of the dynamics near  $L_1$ . That is, when we refer to  $W^c(L_1)$ , or to a normally hyperbolic invariant manifold (obtained by intersecting  $W^c(L_1)$  to an energy level), we consider those manifolds as derived from  $\mathcal{H}_{\text{trunc}}^{(N)}$ . Similarly, the stable and unstable manifolds of a normally hyperbolic invariant manifold, or of its invariant tori, are computed by integrating the equations of motion with initial conditions given by  $\mathcal{H}_{\text{trunc}}^{(N)}$ .

We fix the energy by fixing the Jacobi constant  $C$ . The energy condition  $\{C = c\}$  yields  $J_p$  as an implicit function of  $J_v, \phi_p, \phi_v, c$ . It is known that the restriction of the center manifold  $W_c(L_1)$  to the energy level  $\{C = c\}$  is

a 3-dimensional normally hyperbolic invariant manifold (NHIM):

$$\Lambda_c = W_c(L_1) \cap \{C = c\}.$$

The NHIM can be parametrized by

$$\Lambda_c = \{(J_v, \phi_p, \phi_v)\}.$$

For each fixed value of the vertical action  $J_v = \bar{J} = \text{const.}$ , there is a unique invariant torus for the normal form

$$T_{\bar{J}} = \{(J_v, \phi_p, \phi_v) \in \Lambda_c \mid J_v = \bar{J}\}.$$

Each of these objects  $W^c(L_1)$ ,  $\Lambda_c$ ,  $T_{\bar{J}}$ , have associated stable and unstable (or asymptotic) invariant manifolds of one more dimension than the object itself. The truncated normal form provides a very accurate approximation to the local asymptotic manifolds in a neighborhood of  $L_1$ .

Let  $\Upsilon^s = \Upsilon^u = (0, v)$  be a small interval in the stable (respectively unstable) coordinates  $x_1, y_1$ . (In practice, we take  $v = 10^{-3}$ ). The 4-dimensional local stable and unstable manifolds of  $\Lambda_c$  are given by

$$W_{\text{loc}}^s(\Lambda_c) = \Lambda_c \oplus \Upsilon^s, \quad W_{\text{loc}}^u(\Lambda_c) = \Lambda_c \oplus \Upsilon^u.$$

### 2.3. Scattering Map

One of the main tools that we use in this paper is the scattering map. This is an effective tool to quantify the effect of homoclinic excursions to a NHIM. It can be computed either perturbatively or numerically.

We recall the definition of the scattering map following [6]. We consider a general setting of flow on a manifold  $M$ , and assume that there is a normally hyperbolic invariant manifold  $\Lambda$  for the flow. We will assume that the flow as well as the geometric objects referred to below are differentiable enough, without formulating specific assumptions on regularity. (In the case of the spatial circular RTBP the flow is real analytic, and the geometric objects of interest are at least  $C^1$ -differentiable, but not necessarily analytic.)

As a consequence of normal hyperbolicity, the stable manifold  $W^s(\Lambda)$  and the unstable manifold  $W^u(\Lambda)$  are foliated by stable and unstable manifolds of points  $W^s(y)$ ,  $W^u(y)$ , respectively, for  $y \in \Lambda$ . This implies that for each  $x \in W^u(\Lambda)$  there exists a unique  $x_- \in \Lambda$  such that  $x \in W^u(x_-)$ , and for each  $x \in W^s(\Lambda)$  there exists a unique  $x_+ \in \Lambda$  such that  $x \in W^s(x_+)$ . These

correspondences are described via the *wave maps*  $\Omega_+ : W^s(\Lambda) \rightarrow \Lambda$  given by  $\Omega_+(x) = x_+$ , and  $\Omega_- : W^u(\Lambda) \rightarrow \Lambda$  given by  $\Omega_-(x) = x_-$ , respectively.

Assume that  $W^s(\Lambda)$  and  $W^u(\Lambda)$  intersect transversally along a homoclinic manifold  $\Gamma$ , that is, for each  $x \in \Gamma \subseteq W^u(\Lambda) \cap W^s(\Lambda)$ , we have

$$\begin{aligned} T_x M &= T_x W^u(\Lambda) + T_x W^s(\Lambda), \\ T_x \Gamma &= T_x W^u(\Lambda) \cap T_x W^s(\Lambda). \end{aligned}$$

Further, assume that the intersection of the manifolds satisfy a strong transversality condition, that for each  $x \in \Gamma$  we have

$$\begin{aligned} T_x W^s(\Lambda) &= T_x W^s(x_+) \oplus T_x(\Gamma), \\ T_x W^u(\Lambda) &= T_x W^u(x_-) \oplus T_x(\Gamma). \end{aligned}$$

Then, the restrictions  $\Omega_+^\Gamma, \Omega_-^\Gamma$  of  $\Omega_+, \Omega_-$ , respectively, to  $\Gamma$  are local diffeomorphisms. We can always choose  $\Gamma$  so that  $\Omega_+^\Gamma, \Omega_-^\Gamma$  are diffeomorphisms onto their images. A homoclinic manifold  $\Gamma$  for which the corresponding restrictions of the wave maps to  $\Gamma$  are diffeomorphisms is referred to as a *homoclinic channel*.

**Definition 2.1.** Given a homoclinic channel  $\Gamma$ , the scattering map associated to  $\Gamma$  is the diffeomorphism

$$S^\Gamma = \Omega_+^\Gamma \circ (\Omega_-^\Gamma)^{-1}$$

from the  $\text{Dom}(S^\Gamma) := \Omega_-^\Gamma(\Gamma) \subseteq \Lambda$  to the  $\text{Im}(S^\Gamma) := \Omega_+^\Gamma(\Gamma) \subseteq \Lambda$ .

That is, if  $x \in \Gamma$  is a homoclinic point and  $\Omega_\pm^\Gamma(x) = x_\pm$ , then  $S^\Gamma(x_-) = x_+$ . In general, the domain and range of the scattering map are proper subsets of  $\Lambda$ . There are examples where the local domain of the scattering map cannot be extended to a global one, that is, on the whole  $\Lambda$ , as moving along a loop in  $\Lambda$  leads to lack of monodromy (see [3]).

The scattering map depends on the choice of the homoclinic channel  $\Gamma$ . When we flow the homoclinic channel  $\Gamma$  to  $\Phi^t(\Gamma)$ , the corresponding scattering maps are conjugate by the flow (see [6, Section 2.3]):

$$S^{\Phi^t(\Gamma)} = \phi^t \circ S^\Gamma \circ \phi^{-t}. \quad (4)$$

Of course, when  $\Gamma$  and  $\Phi^t(\Gamma)$  overlap, for  $x \in \Gamma \cap \Phi^t(\Gamma)$ , we have  $S^{\Phi^t(\Gamma)}(x_-) = S^\Gamma(x_-)$ . This means that  $S^\Gamma$  can be continued to  $S^{\Phi^t(\Gamma)}$  for some interval of

times  $t$ , for as long as the corresponding homoclinic channels are well defined and can be continued into one another. We will regard the result of such continuation to the maximal domain as a single scattering map.

When the choice of the homoclinic channel  $\Gamma$  is evident from the context, we drop the superscript from the notation  $S^\Gamma$ .

In the case of a discrete-time dynamical system, the scattering map can be defined in a similar fashion.

A remarkable property of the scattering map is that it is exact symplectic, provided that the manifold and the flow are exact symplectic. We refer to [6] for details.

As we shall see in Section 3.3, in our model we can construct two scattering maps that are defined on a whole annulus inside the NHIM. In this sense, the scattering maps are globally defined on the annulus. Each of this scattering maps is obtained by a continuation of a locally defined scattering map to a maximal domain. In our model, the scattering map extended to its maximal domain satisfies the monodromy condition, as moving around on a non-trivial loop inside the annulus does not yield a multi-valued map.

#### 2.4. Reduction of the Scattering Map to a Poincaré Section

In our previous paper [9], we showed that, in the case of the spatial circular RTBP, the unstable and stable manifolds of  $\Lambda_c$  intersect, giving rise to homoclinic orbits to  $\Lambda_c$ . We can select a homoclinic channel  $\Gamma_c$  and consider the corresponding scattering map

$$S : \text{Dom}(S) \subseteq \Lambda_c \rightarrow \text{Im}(S) \subseteq \Lambda_c.$$

As described in Section 2.3, the scattering map assigns to a point  $x_- \in \Lambda_c$  another point  $x_+ \in \Lambda_c$  whenever there is a homoclinic point  $x \in \Gamma_c$  such that the orbit of  $x$  tends to the orbit of  $x_-$  in the past and to the orbit of  $x_+$  in the future.

To reduce the dimensionality of the scattering map, we consider the Poincaré section  $\Sigma = \{\phi_p = 0\}$ , with associated first return map  $\mathcal{F} : \Sigma \rightarrow \Sigma$ . Let  $\Lambda_c^\Sigma$  denote the intersection of the NHIM with the Poincaré section:

$$\Lambda_c^\Sigma = \Lambda_c \cap \Sigma.$$

The manifold  $\Lambda_c^\Sigma$  is diffeomorphic to the 2-dimensional sphere, and can be parametrized by

$$\Lambda_c^\Sigma = \{(J := J_v, \phi := \phi_v) : J \in [0, J_{max}], \phi \in [0, 2\pi)\},$$

where  $J_{max}$  is given by the energy condition  $\{C = c\}$  and  $J_p = 0$ .

*Remark 1.* In this paper we focus on the action-angle pair  $(J_v, \phi_v)$ . For ease of notation, we will simply write  $(J, \phi)$  for  $(J_v, \phi_v)$ .

We have shown in [9, Section 3.2] that  $\Lambda_c^\Sigma$  is a normally hyperbolic invariant manifold for  $\mathcal{F}$ , which we call the *reduced NHIM*. Accordingly, the full scattering map induces a *reduced scattering map*  $\sigma$ ,

$$\sigma: \text{Dom}(\sigma) \subseteq \Lambda_c^\Sigma \rightarrow \text{Im}(\Lambda_c^\Sigma) \subseteq \Lambda_c^\Sigma.$$

For each fixed value of  $J = \bar{J} = \text{const.}$ , there is a unique invariant curve for the normal form

$$T_{\bar{J}}^\Sigma = \{(J, \phi) \in \Lambda_c \mid J = \bar{J}\}.$$

One can derive the reduced scattering map  $\sigma$  from the full scattering map  $S$  as follows. Let  $x_\pm$  be two points related by the scattering map:  $x_+ = S(x_-)$ . Then we flow  $x_-$  backwards to the Poincaré section  $\Sigma$ , obtaining a new point  $(J_-, \phi_-) \in \Lambda_c^\Sigma$ . Similarly, we flow  $x_+$  forwards to  $\Sigma$ , obtaining  $(J_+, \phi_+) \in \Lambda_c^\Sigma$ . The reduced scattering map  $\sigma$  takes  $(J_-, \phi_-)$  to  $(J_+, \phi_+)$ .

Just like  $S$ , the reduced scattering map  $\sigma$  is also exact symplectic, since it inherits the exact symplectic property from  $\mathcal{F}$ . (See [6]).

*Remark 2.* A scattering map is not unique: it depends on the chosen homoclinic channel. In this paper, we will show that there exist two different channels, and thus two scattering maps defined on a common domain  $\mathcal{A}$  inside the NHIM  $\Lambda_c^\Sigma$ . The domain will be made explicit in Equation (7).

*Remark 3.* When it is clear from the context, we will abbreviate ‘reduced scattering map’ to just ‘scattering map’.

### 2.5. Transition map

From the definition of the scattering map associated to  $\Phi^t$ , it follows that, if  $x \in \Gamma_c$  is a homoclinic point and

$$S(x_-) = x_+, \text{ where } x_\pm \in \Lambda_c$$

then

$$\begin{aligned} d(\Phi^{-t_-}(x), \Phi^{-t_-}(x_-)) &\rightarrow 0, \text{ as } t_- \rightarrow \infty, \\ d(\Phi^{t_+}(x), \Phi^{t_+}(x_+)) &\rightarrow 0, \text{ as } t_+ \rightarrow \infty. \end{aligned}$$

For a given  $\delta > 0$ , we can choose  $T_-, T_+$  as the smallest positive reals  $t_-, t_+$ , respectively, for which

$$d(\Phi^{-t_-}(x), \Phi^{-t_-}(x_-)) < \delta, \quad d(\Phi^{t_+}(x), \Phi^{t_+}(x_+)) < \delta. \quad (5)$$

Thus, the homoclinic orbit segment from  $\Phi^{-T_-}(x)$  to  $\Phi^{T_+}(x)$  is an approximation of the pseudo-orbit  $\Phi^{T_+} \circ S \circ \Phi^{T_-}(x_-)$ . The former is an orbit segment in the manifold  $M_h$ , while the latter is given by an orbit segment of the inner dynamics  $\Phi_{|\Lambda_c}^{T_-}$ , followed by one application of the scattering map  $S$ , followed by another orbit segment of the inner dynamics  $\Phi_{|\Lambda_c}^{T_+}$ .

This correspondence represents the so called *transition map* (see [6]). This is a map  $\tau = \tau_{T_-, T_+}$  defined on a suitable domain in  $\Lambda_c$  given by

$$\tau = \Phi^{T_+} \circ S \circ \Phi^{T_-}.$$

The transition map depends on the choice of the times  $T_-, T_+$ .

In the case of the reduced scattering map – corresponding to the dynamics of the first-return map  $\mathcal{F}$  to the section  $\Sigma$  – the transition map can be defined in a similar fashion. Let  $\hat{x} \in \Gamma_c^\Sigma = \Gamma_c \cap \Sigma$  be a homoclinic point and

$$\sigma(\hat{x}_-) = \hat{x}_+, \quad \text{where } \hat{x}_\pm \in \Lambda_c^\Sigma.$$

In terms of the notation and the coordinates from Section 2.4, we have  $\hat{x}_- = (J_-, \phi_-)$  and  $\hat{x}_+ = (J_+, \phi_+)$ . For a given  $\delta > 0$ , let  $K_-, K_+$  be the smallest positive integers  $k_-, k_+$ , respectively, such that

$$d(\mathcal{F}^{-k_-}(\hat{x}), \mathcal{F}^{-k_-}(\hat{x}_-)) < \delta, \quad d(\mathcal{F}^{k_+}(\hat{x}), \mathcal{F}^{k_+}(\hat{x}_+)) < \delta. \quad (6)$$

Then the transition map is given by

$$\tau = \tau_{K_-, K_+} = \mathcal{F}^{K_+} \circ \sigma \circ \mathcal{F}^{K_-}.$$

Since the dynamics along the hyperbolic manifolds  $W^{u,s}(\Lambda_c^\Sigma)$  is much faster than the inner dynamics  $\mathcal{F}_{|\Lambda_c^\Sigma}$ , it is possible that for some suitable  $\delta$ , in order to satisfy condition (6) one can choose  $K_- = K_+ = 1$ . In this case, the transition map is given by

$$\tau = \tau_{1,1} = \mathcal{F} \circ \sigma \circ \mathcal{F}.$$

Indeed, the transition map used in this paper will be of this type.

In either the flow case or the first return map case, since both the scattering map and the inner dynamics are exact symplectic, it follows that the transition map is also exact symplectic (see [6]).



### 3. Numerical Scattering Map on a Grid for $C = 3.00088$

Using the methodology presented in our previous paper [9], we compute an accurate numerical approximation to the NHIM  $\Lambda_c$  and its stable/unstable manifolds. In this section, we show that the asymptotic manifolds intersect transversally along two homoclinic channels, giving rise to two different scattering maps. We compute the scattering maps numerically at a grid of points; they are shown in Figure 9.

For the purpose of this paper we will use the energy value  $C = c := 3.00088$ . This value is chosen after the appearance of the equilibrium point  $L_1$  ( $c_1 := 3.00090$ ), but before the appearance of *halo* orbits ( $c_{\text{halo}} := 3.00082$ ). The choice of energy is motivated by two reasons.

Firstly,  $c$  is close enough to  $c_1$  so that the dynamics around  $L_1$  is almost integrable. Thus, the (integrable) Birkhoff normal form  $H_{\text{trunc}}^{(N)}$  provides a good approximation to the local dynamics. (Remark 4 quantifies the normal form error).

Secondly,  $c$  is close enough to  $c_1$  so that we are in the setting of *a priori chaotic Arnold diffusion* (see, e.g., [29]). Assume that for the exact RTBP (not the truncated normal form) there exists a NHIM that is close to  $\Lambda_c$ , and is almost filled with invariant tori. (This was proven for the planar RTBP in [43]). Then the tori do not separate the phase space, so there may exist trajectories that escape a given neighborhood of  $L_1$ . Proving the existence of such orbits is a classical problem that has attracted lots of attention.

In this paper, we provide new tools to study the problem of Arnold diffusion. We hope that this will lead to the explicit construction of diffusion orbits, as well as explicit bounds on their diffusion time.

Fixing the energy value  $c = 3.00088$ , the NHIM  $\Lambda_c$  consists of a continuous family of 2-dimensional invariant tori around  $L_1$ , which we parametrize by the vertical action  $J$ . The vertical action increases along the family from  $J = 0$  to  $J = J_{\text{max}} := 0.052$ . Correspondingly, the planar action  $J_p$  decreases from 0.05029 to 0.

Figure 3 shows some tori in the NHIM  $\Lambda_c$ .

- $J = 0$  (i.e.  $J_p = 0.05029$ ) corresponds to the unique planar Lyapunov orbit in this energy level.
- $J = 0.052$  (i.e.  $J_p = 0$ ) corresponds to the unique vertical Lyapunov orbit in this energy level.

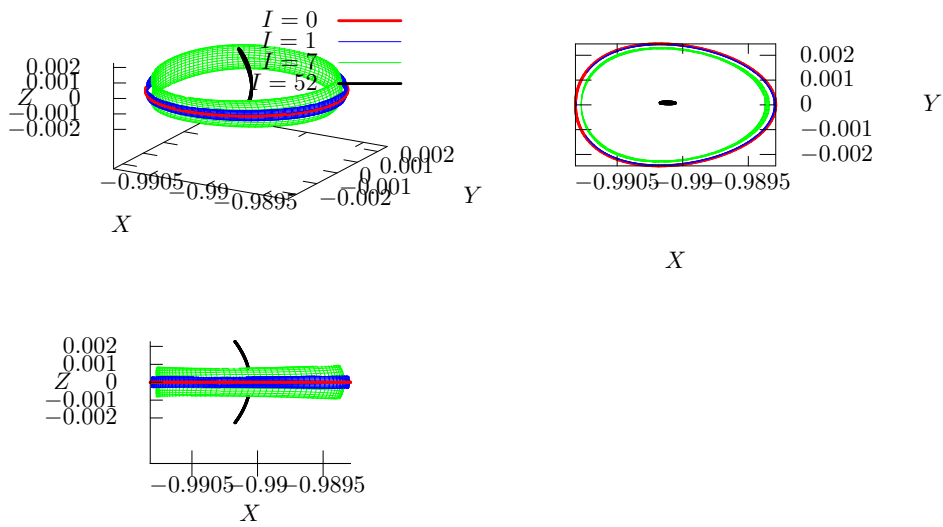


Figure 3: The NHIM  $\Lambda_c$  consists of a continuous family of invariant tori around  $L_1$ . The endpoints of the family are the planar and vertical Lyapunov orbits (shown in red and black, respectively). In between, there are 2-d tori of increasing vertical amplitude  $J$ . (For clarity, only two of them are shown). The transfer trajectory shown in Figure 1 starts at an initial condition very close to the blue torus  $I = 1$  and ends very close to the green torus  $I = 7$ .

- Every intermediate action  $J \in (0, 0.052)$  corresponds to a 2-dimensional torus located between the planar and the vertical Lyapunov orbits.

As seen in Figure 3, the NHIM  $\Lambda_c$  spans a spherical region of radius 0.002 Astronomical Units (AU), or roughly 300000 km around the equilibrium point  $L_1$ .

*Remark 4.* The accuracy of the Birkhoff Normal Form (BNF) expansion has been tested against numerical integration of the RTBP equations, following the same procedure as in [40]. Compute an initial condition on  $\Lambda_c$  by evaluating the BNF up to order  $N = 16$ . This initial condition is integrated for  $\pi$  units of adimensional time using two different methods:

1. Using the BNF. No numerical integration is needed. As the Hamiltonian is integrable, and we have it integrated, we simply tabulate the solution at time  $\pi$ .
2. Integrate the RTBP equations using a Runge-Kutta-Feldberg numerical integrator of order 7-8, with local error at each step within  $10^{-14}$ .

Then compare the two final conditions.

This test has been performed for several initial conditions on  $\Lambda_c$ . In all cases, the difference in the Euclidean norm for the final condition is less than  $10^{-12}$  adimensional RTBP units. Thus the initial condition was very accurate, in the sense that it is very close to one of the tori computed by the BNF.

In fact, it is known that, due to the hyperbolicity of orbits around the collinear point, errors increase by a factor close to 1500 after  $\pi$  units of time. Therefore the error in the initial condition is less than  $10^{-12}/1500$  adimensional units, close to machine precision.

### 3.1. Homoclinic Orbits

In [9], Section 4.3, we explained in detail how to compute the intersection of the stable and unstable manifolds  $W^s(\Lambda_c) \cap W^u(\Lambda_c)$  restricted to a suitable surface of section  $\mathcal{S}$ .

Using this procedure, we find that the asymptotic manifolds do indeed intersect transversally, giving rise to families of homoclinic orbits from  $\Lambda_c$  to itself. These homoclinics will later be encoded in two scattering maps.

Roughly speaking, the numerical procedure to compute each homoclinic consists of finding two initial conditions  $y_-, y_+$  on the *local* unstable resp. stable manifolds, and a point  $x \in \mathcal{S}$  such that: (1)  $\Phi^t(y_-) = x$ ; and (2)

$\Phi^{-s}(y_+) = x$ . Then  $x$  is a homoclinic point, generating a homoclinic orbit segment from  $y_-$  to  $y_+$ .

We would like to emphasize some aspects of this computation:

- The initial conditions  $y_-, y_+$  are taken at a distance  $v = 10^{-3}$  of the NHIM along the unstable/stable coordinates. This guarantees that they are inside the domain where the normal form is accurate.
- At the same time, these initial conditions are sufficiently far from the NHIM so that the homoclinic orbit segment does not wind around  $L_1$  more than once.
- All homoclinics take  $5.936738 \leq t + s \leq 6.000688$  time units to go from  $y_-$  to  $y_+$ . We will refer to  $t + s$  as the ‘flight time’ of the homoclinic. The shortest and longest flight times correspond to the two homoclinics of the Lyapunov orbit. See Figure 4.

*Remark 5.* The section  $\mathcal{S}$  corresponds to crossing the  $XZ$ -plane (with positive  $Y$  velocity) in co-rotating SCRTBP coordinates. The choice of the section is somewhat arbitrary; it is only related to the numerical computation. We consider **only the first intersection** of the stable and unstable manifolds with  $\mathcal{S}$ . The ‘primary’ homoclinic connections generated in this way travel around the Earth once. There exist subsequent (second, third, etc.) intersections with  $\mathcal{S}$ , but they are not as interesting for applications, since these homoclinic connections are longer (they travel around the Earth twice, thrice, etc.). For more details, see [9, Section 4.3].

Following the decomposition of  $\Lambda_c$  into invariant tori, we first study homoclinic orbits from each  $T_J$  to itself. Later we will study homoclinic orbits from  $T_J$  to all nearby tori.

- When  $J = 0$ , the invariant manifolds  $W^u(T_0)$  and  $W^s(T_0)$  have two transverse intersections in the section  $\mathcal{S}$ . That is, the planar Lyapunov orbit  $T_0$  has two homoclinic connections with itself. See Figure 4.
- For every fixed  $J \in (0, 0.01)$ , the invariant manifolds  $W^u(T_J)$  and  $W^s(T_J)$  have eight transverse intersections. That is, every torus  $T_J$  in this domain has eight homoclinic connections with itself.

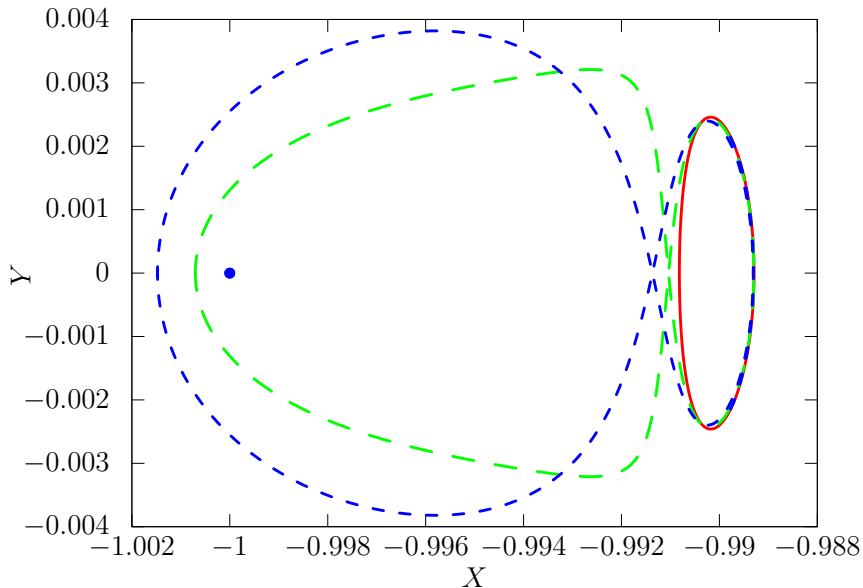


Figure 4: Planar Lyapunov orbit (solid line), and its two ‘primary’ homoclinics (dashed). Both homoclinics travel around the Earth once (located at  $X = -1 + \mu$ ).

- In contrast, for action values  $J$  above 0.01, the invariant manifolds  $W^u(T_J)$  and  $W^s(T_J)$  cease to intersect (at their first intersection with the section  $\mathcal{S}$ ).

*Remark 6.* The planar Lyapunov orbit has two ‘primary’ homoclinics that travel around the Earth (see Figure 4). However, one of them makes a longer excursion than the other: the green homoclinic has flight time 5.936738, while the blue one has flight time 6.000688.

*Remark 7.* Each of the two intersections in  $W^u(T_0) \cap W^s(T_0)$  gives rise to four intersections when we increase the dimension of the manifolds  $W^u(T_J), W^s(T_J)$  by one. This is expected by Morse theory [44].

Every transverse intersection

$$x \in W^u(T_J) \cap W^s(T_J)$$

implies that there exists a pair of points  $x_-, x_+ \in T_J$  such that  $W^u(x_-)$  intersects  $W^s(x_+)$  at the homoclinic point  $x$ . Since this is an open condition, we can define a local scattering map on some open set containing  $x_-$  by  $x_- \mapsto S(x_-) := x_+$ .

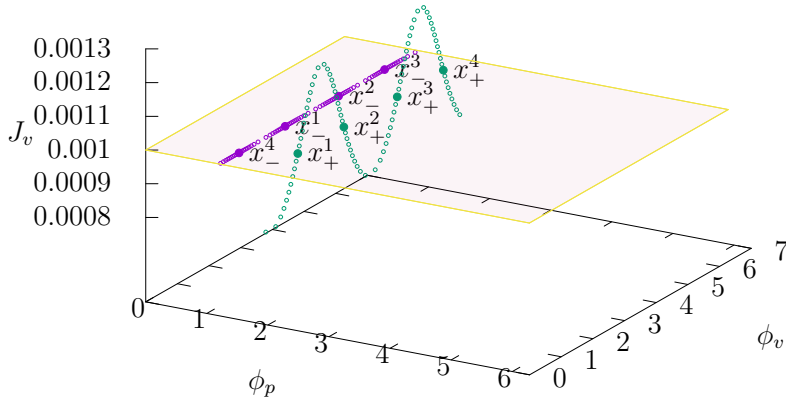


Figure 5: Action of the scattering map  $S_1$  on the torus  $T_J$  with  $J = 0.001$ .  $S_1$  maps the purple set to the green set. When the ‘source’ and ‘destination’ tori  $T_J$  have the same action ( $J = 0.001$  in this picture, corresponding to the translucent plane),  $S_1$  maps the four points  $x_-^i \in T_J$  to  $x_+^i \in T_J$ . Fixing the source torus  $T_J$  and varying the destination torus  $T_{J'}$  to action levels  $J'$  near  $J$ , the scattering map  $S_1$  is continued to the purple and green sets.

In fact, we find that these local scattering maps can be continued to form two *global* scattering maps, which we will denote  $S_1$  and  $S_2$ . They determine the reduced scattering maps,  $\sigma_1$  and  $\sigma_2$  (see Section 2.4).

### 3.2. Extending the Scattering Map

Let us explain how  $S_1$  is numerically constructed. ( $S_2$  is constructed analogously). The general idea is to compute  $S_1$  on several tori  $T_J$  (for example  $J = 0.001, 0.002, \dots, 0.007$ ). Given that the NHIM  $\Lambda_c$  is the union of all tori, this provides a coarse representation of  $S_1$  on a whole annulus  $\mathcal{A}$  inside  $\Lambda_c$  (see Equation (7)).

To compute  $S_1$  on a given torus  $T_J$ , fix an action  $J \in (0, 0.007]$ . As explained above,  $W^u(T_J)$  has eight transverse intersections with  $W^s(T_J)$  in the surface of section  $\mathcal{S}$ . Four of them, which we will denote  $x^i$  for  $i = 1, 2, 3, 4$ , give rise to four pairs of points associated by the local scattering

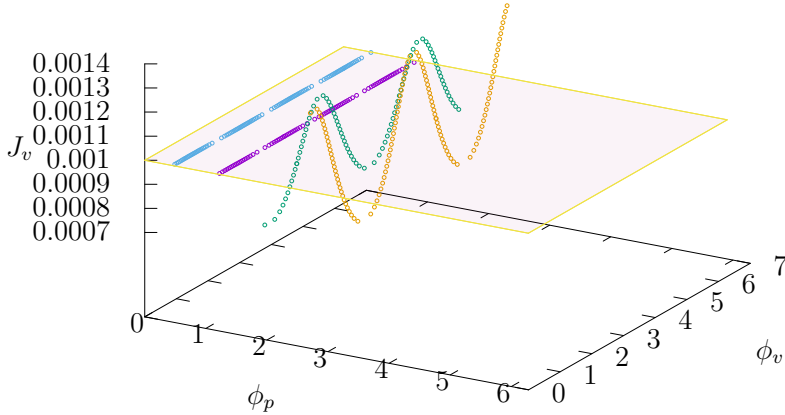


Figure 6: Action of scattering maps  $S_1$  and  $S_2$  on the torus  $T_J$  with  $J = 0.001$ .  $S_1$  maps the purple set to the green set, while  $S_2$  maps blue to orange.

maps:

$$x_+^i = S(x_-^i) \quad \text{for } i = 1, \dots, 4.$$

Figure 5 shows these four pairs of points:  $x_-^i$  in the domain are plotted in purple, while  $x_+^i$  in the codomain are plotted in green.

Keeping the action of the source torus fixed to  $J$ , vary the action of the destination torus to a new value  $J'$  close to  $J$ , and recompute the intersection  $W^u(T_J) \cap W^s(T_{J'})$ , giving rise to four new homoclinic points and four corresponding pairs of points associated by  $S_1$ . Continue this procedure until the manifolds  $W^u(T_J)$  and  $W^s(T_{J'})$  cease to intersect, effectively extending the domain of the scattering map  $S_1$  from four points to the purple set in Figure 5, and the codomain to the green set.

The continuation procedure is actually performed in two directions: First increase  $J'$  from  $J$ , producing the portion of the green set located above the translucent plane, until the manifolds cease to intersect ( $J' \approx 0.00125$  in the Figure). Then decrease  $J'$  from  $J$ , producing the portion below the plane, until the manifolds cease to intersect ( $J' \approx 0.0008$  in the Figure).

*Remark 8.* Starting with the other four homoclinic points,  $x^i$  for  $i = 5, 6, 7, 8$ , and applying the same procedure, gives rise to a different scattering map  $S_2$ .

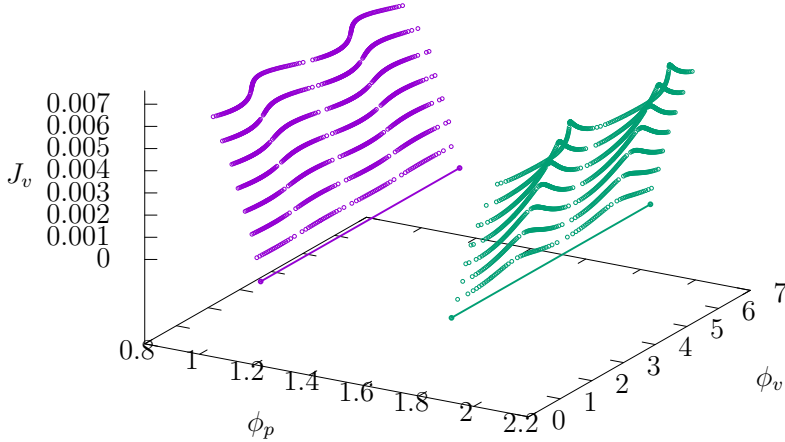


Figure 7:  $S_1$  acting on several action levels:  $J = 0.001, 0.002, \dots, 0.007$ .

See Figure 6.  $S_1$  and  $S_2$  are fundamentally different, they are not conjugated by the flow (see (4)).

Finally, we repeat this procedure for several tori ( $J = 0.001, 0.002, \dots, 0.007$ ). See Figure 7.

*Remark 9.* As  $J \rightarrow 0$ , the torus  $T_J$  degenerates into the horizontal Lyapunov periodic orbit  $T_0$ . The four homoclinic points  $x^i$  converge to a single homoclinic point  $x$  for  $T_0$ . Similarly, the four pairs  $x^i_-, x^i_+$  converge to a single pair  $x_-, x_+$  of points associated by  $S_1$ . Figure 7 shows  $x_-, x_+$  as straight lines (all angles  $\phi_v \in [0, 2\pi)$  are identified for  $J = 0$ ).

Notice that one could extend  $S_1$  from the purple set to the whole NHIM  $\Lambda_c$  using the conjugacy property of the scattering map by the flow (4). However, we will use the reduced scattering map  $\sigma_1$  instead. Recall from Section 2.4 that the reduced scattering map can be obtained from the full scattering map simply by flowing the points  $x_-/x_+$  backwards/forwards to the Poincaré section  $\Sigma = \{\phi_p = 0\}$ .

Flowing the purple set backwards to  $\Sigma$ , we obtain a mesh  $\{(J, \phi)\}$  discretizing the reduced NHIM  $\Lambda_c^\Sigma$ . Flowing the green set forwards to  $\Sigma$ , we obtain the image set  $\{(J', \phi')\}$  under  $\sigma_1$ , also on  $\Lambda_c^\Sigma$ . This way, we have



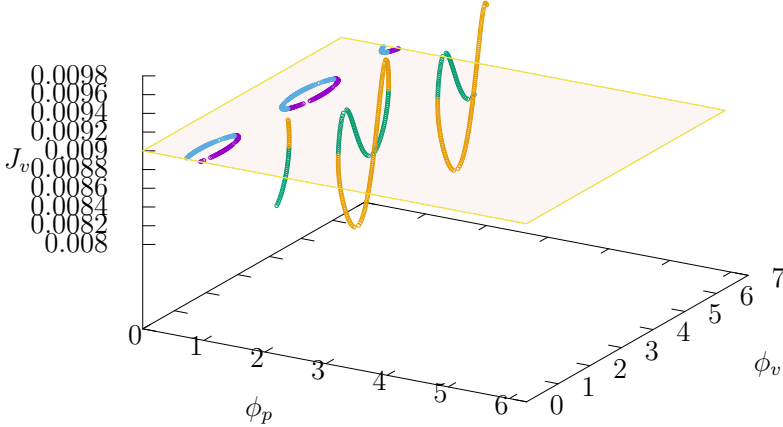


Figure 8: Action of scattering maps  $S_1$  and  $S_2$  on the action level  $J = 0.009$ .  $S_1$  and  $S_2$  have “merged”, and they can not be extended to the whole torus.

extended the local scattering maps onto a global (reduced) scattering map  $\sigma_1$  on  $\Lambda_c^\Sigma$ .

Figure 9 (top panel) shows the image set of the global scattering map  $\sigma_1$ . For example, the green set in Figure 5 ( $J = 0.001$ ) corresponds to the lowest curve in Figure 9 after flowing it forwards.

### 3.3. Domain of the Global Scattering Map

As discussed above, the global scattering maps  $\sigma_1, \sigma_2$  are well defined on an annulus  $\mathcal{A}$  inside  $\Lambda_c^\Sigma$  given by

$$\mathcal{A} = \{(J, \phi) : J \in (0, 0.007] \text{ and } \phi \in [0, 2\pi)\}. \quad (7)$$

For  $0.007 < J < 0.01$ , we find that the scattering maps can not be defined on the whole torus  $T_J$ . For illustration, Figure 8 shows the continuation of all eight local scattering maps when  $J = 0.009$ . Notice that the purple and blue sets (which belong to the domain of  $S_1$  and  $S_2$  respectively) have become connected, and they form two contractible circles. Moreover, the purple and blue sets do not cover all angles  $\phi_v \in [0, 2\pi)$  as before. Thus one can not extend  $S_i$  to the whole torus  $T_J$  by the flow using the conjugacy

property (4). Equivalently, the reduced scattering map  $\sigma_i$  is not defined on the whole invariant curve  $T_J^\Sigma$ .

For the purpose of this paper, we will restrict the domain of the global scattering maps  $\sigma_1, \sigma_2$  to the annulus  $\mathcal{A}$ .

*Remark 10.* The domain  $\mathcal{A}$  is quite large, in the sense that it contains most actions  $J \in [0, 0.01]$  for which there exist ‘primary’ homoclinics.

#### 4. Series Representation of the Scattering Map

The goal of this section is to introduce a series representation of the (global, reduced) scattering maps  $\sigma_1$  and  $\sigma_2$ . This finite series expansion consists in Equations (9)-(11) and (15) below. It is a more efficient representation than the numerical scattering map computed in the previous section, since it is limited to a small number of terms. Moreover, it allows us to evaluate  $\sigma$  at any point of its domain.

As it turns out,  $J$  and  $\phi$  have different scales:  $J$  is of order  $10^{-3}$ , while  $\phi$  is order 1. In order to improve numerical conditioning, it is convenient to scale the  $J$  coordinate as follows:

$$I = 1000J. \tag{8}$$

From now on, we will work with the scaled coordinate  $I$  instead of  $J$ .

The most classical way to represent a symplectic map  $(I, \phi) \rightarrow (I', \phi')$  is by a generating function depending on old and new variables. In [12], the scattering map on Lyapunov periodic orbits was shown to be a phase shift  $(I, \phi) \rightarrow (I, \phi + \Delta(I))$ . Thus, in our setting it is natural to look for a generating function of the form

$$\mathcal{L}(I, \phi') = I\phi' + \Omega(I) + \tilde{\mathcal{L}}(I, \phi'),$$

which will at least be valid for small values of  $I$ . The generating function  $\mathcal{L}(I, \phi')$  is split into its average term (with respect to  $\phi'$ )  $\Omega(I)$  and its oscillatory term  $\tilde{\mathcal{L}}(I, \phi')$ , satisfying  $\int_0^{2\pi} \tilde{\mathcal{L}}(I, \phi') d\phi' = 0$ .

Hence, the equations for the scattering map  $(I', \phi') = \sigma(I, \phi)$  are given implicitly by

$$\phi = \frac{\partial \mathcal{L}}{\partial I}(I, \phi') = \phi' + \omega(I) + \frac{\partial \tilde{\mathcal{L}}}{\partial I}(I, \phi') \tag{9a}$$

$$I' = \frac{\partial \mathcal{L}}{\partial \phi'}(I, \phi') = I + \frac{\partial \tilde{\mathcal{L}}}{\partial \phi'}(I, \phi'), \tag{9b}$$

where  $\omega(I) = \Omega'(I)$ .

We will approximate both  $\tilde{\mathcal{L}}(I, \phi')$  and  $\omega(I)$  in Equation (9) using finite series expansions. Firstly, we approximate the function  $\tilde{\mathcal{L}}(I, \phi')$  using a Fourier-Taylor expansion

$$\tilde{\mathcal{L}}(I, \phi') = - \sum_{n=1}^N \frac{B_n(I)}{n} \cos n\phi' + \sum_{n=1}^N \frac{A_n(I)}{n} \sin n\phi', \quad (10)$$

where

$$A_n(I) = \sum_{l=0}^L a_l^{(n)} I^l \quad \text{and} \quad B_n(I) = \sum_{l=0}^L b_l^{(n)} I^l. \quad (11)$$

The goal is to find the coefficients  $a_l^{(n)}$  and  $b_l^{(n)}$ . In Section 3, we obtained numerically the scattering map  $\sigma$  on a grid of equispaced  $(I, \phi)$  points. See Figure 9. It is a simple matter to fit the coefficients to this data, as explained in Section 4.1.

*Remark 11.* The spatial RTBP is invariant with respect to the transformation  $(Z, \dot{Z}) \rightarrow (-Z, -\dot{Z})$ . Thus, every trajectory passing through the point  $(X, Y, Z)$  has a *symmetric trajectory with respect to the XY plane*, which passes through the point  $(X, Y, -Z)$ . In particular, every heteroclinic trajectory from torus  $I$  to torus  $I'$  has a symmetric heteroclinic trajectory from torus  $I$  to  $I'$ . In normal form coordinates, the symmetry  $Z \rightarrow -Z$  corresponds to  $\phi_v \rightarrow \phi_v + \pi$ . This translates to the following fact for the scattering map of the flow. Suppose that  $S(J_v, \phi_p, \phi_v) = (J'_v, \phi'_p, \phi'_v)$ . Then we have  $S(J_v, \phi_p, \phi_v + \pi) = (J'_v, \phi'_p, \phi'_v + \pi)$ . Equivalently for the reduced scattering map: Suppose that  $\sigma(I, \phi_v) = (I', \phi'_v)$ . Then we have  $\sigma(I, \phi_v + \pi) = (I', \phi'_v + \pi)$ . This implies that the image under the scattering map of any torus is a  $\pi$ -periodic curve (see Figure 9). Indeed, we have checked that the curves in Figure 9 are  $\pi$ -periodic up to a tolerance of  $10^{-6}$ . From this point on, **we will plot all figures involving  $\phi_v$  in the domain  $[0, \pi)$  only.**

#### 4.1. Fourier-Taylor Approximation of the Generating Function

Let  $I$  be fixed, and consider equation (9b):

$$I' = I + \frac{\partial \tilde{\mathcal{L}}}{\partial \phi'},$$

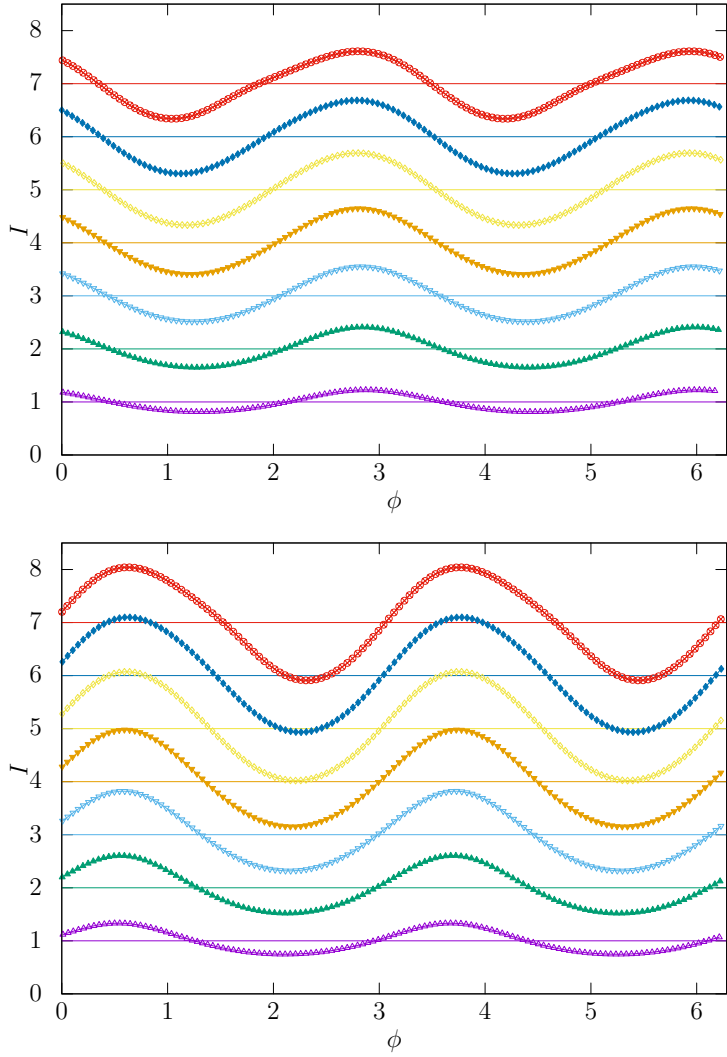


Figure 9: Image under the scattering map of several tori ( $I = 1, 2, \dots, 7$ ). Above: action of  $\sigma_1$ , below: action of  $\sigma_2$ . A torus  $\{(I, \phi) : I = \text{const}, \phi \in [0, 2\pi)\}$  and its image are plotted using the same color. Notice that the curves are  $\pi$ -periodic.

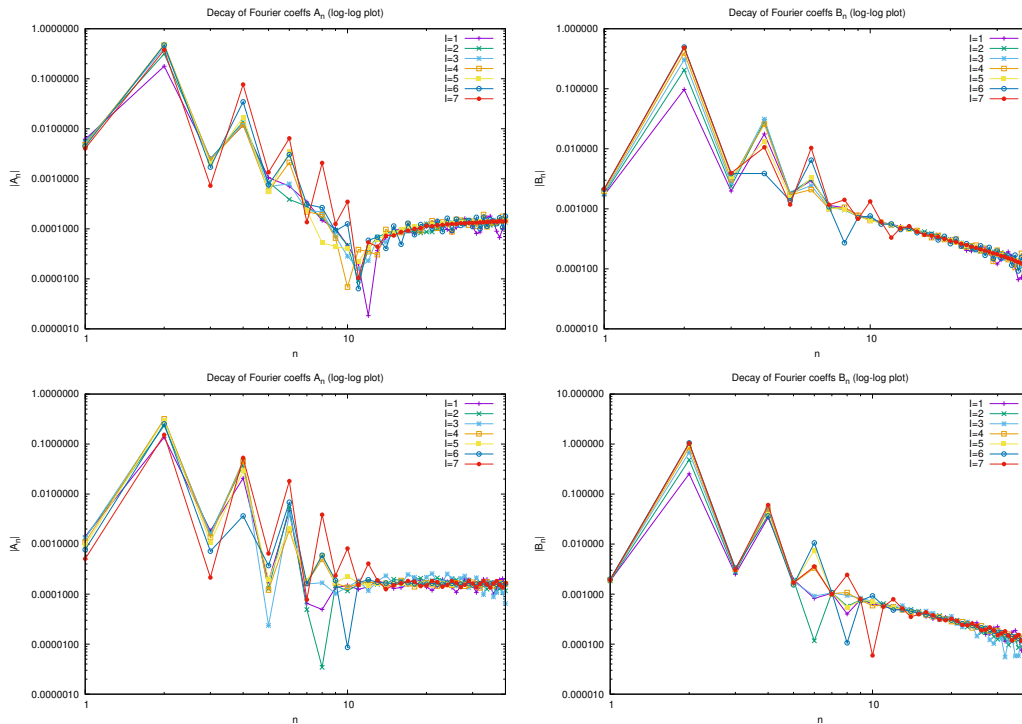


Figure 10: Decay of Fourier coefficients (log-log plot) for the scattering map  $\sigma_1$  (above) and  $\sigma_2$  (below).

where

$$\frac{\partial \tilde{\mathcal{L}}}{\partial \phi'} = \sum_{n=1}^N A_n \cos n\phi' + \sum_{n=1}^N B_n \sin n\phi'. \quad (12)$$

Given a set of  $(I', \phi')$  values on a grid (data points composing one curve in Figure 9), we use the discrete Fourier transform to obtain the Fourier coefficients  $A_n, B_n$ .

*Remark 12.* Since we have 128  $(I', \phi')$  data points for each torus, the maximum possible degree of the Fourier expansion (10) is  $N = 64$ .

Next, let  $I$  vary to obtain the Fourier coefficients  $A_n(I), B_n(I)$  for each torus  $I = 1, 2, \dots, 7$ . Figure 10 shows the decay of these Fourier coefficients for each torus.

*Remark 13.* We know from Remark 11 that the scattering map is  $\pi$ -periodic. Thus, for each torus  $I = \text{const}$ , its image is a  $\pi$ -periodic curve  $I' = \gamma(\phi')$ , and the odd Fourier coefficients should all be zero:  $A_{2k+1}(I) = B_{2k+1}(I) = 0$

for  $k = 0, 1, 2, \dots$ . Of course, in Figure 10 they are not exactly zero because the numerical data is not exactly  $\pi$ -periodic. From now on, all odd Fourier coefficients are set to zero, to obtain a model that satisfies the theoretical  $\pi$ -periodicity of the scattering map.

Let now the index  $n$  of the Fourier coefficient be fixed, and consider the Taylor (polynomial) approximation of  $A_n(I)$  and  $B_n(I)$  given in equation (11). Alternatively, given a set of  $L+1$  data points  $(I_0, A_n(I_0)), \dots, (I_L, A_n(I_L))$ , we will express the polynomials (11) in Newton's form

$$A_n(I) = \sum_{l=0}^L \tilde{a}_l^{(n)} N_l(I) \quad \text{and} \quad B_n(I) = \sum_{l=0}^L \tilde{b}_l^{(n)} N_l(I), \quad (13)$$

where  $\tilde{a}_l^{(n)}, \tilde{b}_l^{(n)}$  are the *divided differences*, and  $N_l(I)$  are Newton's basis polynomials

$$N_0(I) = 1, \quad N_l(I) := \prod_{i=0}^{l-1} (I - I_i) \quad \text{for } l = 1, \dots, L.$$

Given the values  $A_n(I)$  at  $I = 0, 1, 2, \dots, 7$  obtained in the previous step (resp.  $B_n(I)$ ), we use polynomial interpolation (Newton's 'divided differences' algorithm) to obtain the coefficients  $\tilde{a}_l^{(n)}$  (resp.  $\tilde{b}_l^{(n)}$ ). The divided differences of the first eight Fourier coefficients are listed in Table 1.

*Remark 14.* Since we only have 8 data points for each Fourier coefficient, the maximum possible degree of the Newton expansion (13) is  $L = 7$ .

*Remark 15.* The constant terms  $\tilde{a}_0^{(n)}, \tilde{b}_0^{(n)}$  of the Newton expansion are all zero, since  $\tilde{a}_0^{(n)} = A_n(0) = 0$  and  $\tilde{b}_0^{(n)} = B_n(0) = 0$  for all  $n$ .

#### 4.2. Taylor Approximation of the Frequency $\omega(I)$

Finally, we approximate the frequency  $\omega(I)$  in Equation (9).

*Frequency  $\omega(I)$  at  $I = 1, 2, \dots, 7$*

For action levels  $I = 1, 2, \dots, 7$  we have scattering data  $(I, \phi) \rightarrow (I', \phi')$  available, and the frequency  $\omega(I)$  can be obtained from Equation (9a) as

$$\omega(I) = \phi - \phi' - \frac{\partial \tilde{\mathcal{L}}}{\partial I}(I, \phi'). \quad (14)$$

In an exact calculation,  $\omega(I)$  should be independent of  $\phi$ . Numerically, using Equation (14) to approximate the value of  $\omega(I)$  would yield slightly different

$n$	$\tilde{a}_1^{(n)}$	$\tilde{a}_2^{(n)}$	$\tilde{a}_3^{(n)}$	$\tilde{a}_4^{(n)}$	$\tilde{a}_5^{(n)}$	$\tilde{a}_6^{(n)}$	$\tilde{a}_7^{(n)}$
2	<b>0.178180</b>	<b>-0.020025</b>	0.000401	-0.000251	0.000046	0.000019	-0.000022
4	0.011726	-0.004878	0.001114	-0.000129	0.000039	-0.000006	0.000001
6	0.000712	-0.000519	0.000295	-0.000065	0.000004	-0.000000	-0.000001
8	0.000147	-0.000064	0.000027	-0.000012	0.000002	0.000000	0.000000

$n$	$\tilde{b}_1^{(n)}$	$\tilde{b}_2^{(n)}$	$\tilde{b}_3^{(n)}$	$\tilde{b}_4^{(n)}$	$\tilde{b}_5^{(n)}$	$\tilde{b}_6^{(n)}$	$\tilde{b}_7^{(n)}$
2	<b>-0.097275</b>	-0.005156	0.002856	-0.000574	0.000143	0.000003	-0.000016
4	-0.017677	0.003403	0.000242	-0.000067	0.000004	-0.000000	-0.000003
6	-0.002965	0.001408	-0.000332	0.000035	-0.000008	0.000002	-0.000000
8	-0.001045	0.000566	-0.000206	0.000053	-0.000009	0.000002	-0.000000

(a) Scattering map  $\sigma_1$ .

$n$	$\tilde{a}_1^{(n)}$	$\tilde{a}_2^{(n)}$	$\tilde{a}_3^{(n)}$	$\tilde{a}_4^{(n)}$	$\tilde{a}_5^{(n)}$	$\tilde{a}_6^{(n)}$	$\tilde{a}_7^{(n)}$
2	<b>0.136664</b>	<b>-0.019375</b>	0.001251	-0.001067	0.000499	-0.000153	0.000031
4	-0.020745	0.001757	0.000921	-0.000221	0.000089	-0.000028	0.000006
6	-0.004644	0.001886	-0.000222	-0.000027	-0.000001	0.000001	-0.000000
8	-0.000049	0.000048	-0.000051	0.000015	0.000000	0.000000	-0.000000

$n$	$\tilde{b}_1^{(n)}$	$\tilde{b}_2^{(n)}$	$\tilde{b}_3^{(n)}$	$\tilde{b}_4^{(n)}$	$\tilde{b}_5^{(n)}$	$\tilde{b}_6^{(n)}$	$\tilde{b}_7^{(n)}$
2	<b>0.253827</b>	<b>-0.011566</b>	-0.001286	0.000406	-0.000226	0.000067	-0.000018
4	0.034009	-0.008888	0.000925	-0.000160	0.000086	-0.000022	0.000006
6	0.000823	-0.000764	0.000505	-0.000121	0.000025	-0.000008	0.000001
8	0.000400	-0.000113	0.000069	-0.000035	0.000007	0.000000	0.000000

(b) Scattering map  $\sigma_2$ .

Table 1: Divided differences  $\tilde{a}_i^{(n)}$ ,  $\tilde{b}_i^{(n)}$  of the first Fourier coefficients  $A_n(I)$ ,  $B_n(I)$ . All odd Fourier coefficients are zero and thus not listed (see Remark 13). All constant terms of the Newton expansion  $\tilde{a}_0^{(n)}$ ,  $\tilde{b}_0^{(n)}$  are zero, and thus not listed (see Remark 15). Notice that the two coefficients  $\tilde{a}_1^2$  and  $\tilde{b}_1^2$  (in red) are much larger than the rest of coefficients for both scattering maps  $\sigma_1$ ,  $\sigma_2$ . For the scattering map  $\sigma_1$ , the coefficient  $\tilde{a}_2^2$  (in blue) is much larger than the rest of coefficients in the last six columns, i.e.  $\tilde{a}_j^n$  for  $j \geq 2$ . For the scattering map  $\sigma_2$ , the two coefficients  $\tilde{a}_2^2$  and  $\tilde{b}_2^2$  are much larger than the rest with  $j \geq 2$ .

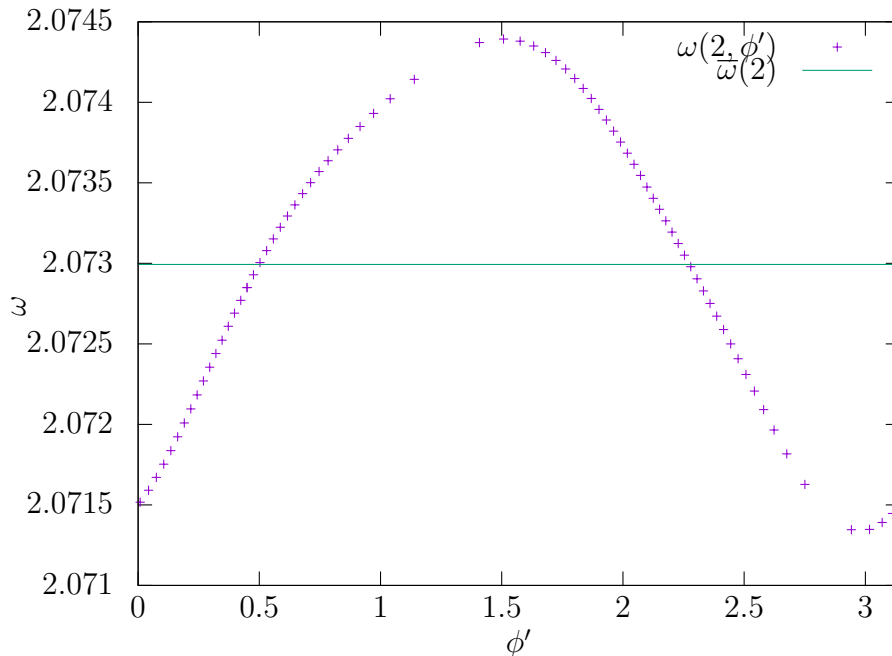


Figure 11: Function  $\omega(I = 2, \phi')$ . In an exact calculation,  $\omega(I, \phi')$  should be constant and equal to the average  $\bar{\omega}(I)$ .

Figure 12: Frequency function  $\omega(I)$  for  $\sigma_1$  (in green) and  $\sigma_2$  (yellow).

values for  $\omega(I)$  depending on the data point  $(I, \phi)$ , and indeed depending on  $\phi$ . Thus, we will compute  $\omega(I)$  as the *average* of Equation (14) over all  $\phi \in [0, 2\pi)$ .

To give an idea of the numerical error in determining  $\omega(I)$ , Figure 11 compares the frequency  $\omega(2, \phi')$  of torus  $I = 2$  to its average  $\bar{\omega}$  over all available  $\phi'$  values. Their discrepancy is less than 0.002 radians.

#### *Frequency $\omega(I)$ at an arbitrary $I$ -value*

Similarly to what we did in Section 4.1 with the Fourier coefficients  $A_n(I)$ ,  $B_n(I)$ , we use the Newton series representation of  $\omega(I)$ :

$$\omega(I) = \sum_{l=0}^L \tilde{c}_l N_l(I). \quad (15)$$



$\tilde{c}_0$	$\tilde{c}_1$	$\tilde{c}_2$	$\tilde{c}_3$	$\tilde{c}_4$	$\tilde{c}_5$	$\tilde{c}_6$
<b>2.027748</b>	<b>0.046673</b>	0.001164	0.000489	-0.000046	0.000016	0.000003

(a) Scattering map  $\sigma_1$ .

$\tilde{c}_0$	$\tilde{c}_1$	$\tilde{c}_2$	$\tilde{c}_3$	$\tilde{c}_4$	$\tilde{c}_5$	$\tilde{c}_6$
<b>3.555994</b>	<b>-0.046434</b>	-0.001651	-0.000143	-0.000115	0.000046	-0.000026

(b) Scattering map  $\sigma_2$ .

Table 2: Divided differences  $\tilde{c}_l$  of function  $\omega(I)$ . Notice that the coefficient  $\tilde{c}_0$  (in red) is much larger than the rest of coefficients of this table, and larger than those of Table 1, for both scattering maps  $\sigma_1$  and  $\sigma_2$ . Notice also that  $\tilde{c}_1$  (in blue) is much larger than the rest of coefficients of the last five columns, i.e  $\tilde{c}_j$  for  $j \geq 2$ , of this table, and larger than the double of those coefficients of the last 6 columns of Table 1 for both scattering maps  $\sigma_1$  and  $\sigma_2$ .

Given the values  $\bar{\omega}(I)$  at  $I = 1, 2, \dots, 7$  obtained in the previous step, we use polynomial interpolation to obtain the coefficients  $c_l$ . The frequency function  $\omega(I)$  is plotted in Figure 12.

*Remark 16.* Since we only have 7 data points for  $\omega$ , the maximum possible degree of the Newton expansion (15) is  $L = 6$ .

This completes the series representation of the scattering map, consisting of Equations (10)-(11) and (15).

#### 4.3. Applying the Scattering Map

We plan to use equations (9) to apply the scattering map  $(I', \phi') = \sigma(I, \phi)$ . However, it must be stressed that these equations do not give  $I', \phi'$  *explicitly* as functions of  $I, \phi$ . On the contrary,  $I', \phi'$  are given *implicitly*. However,  $\phi'$  can be obtained from Equation (9a) as a fixed point of

$$\phi' = f(\phi'; I, \phi) = \phi - \omega(I) - \frac{\partial \tilde{\mathcal{L}}}{\partial I}(I, \phi').$$

We simply use fixed point iteration, starting with the initial approximation  $\phi'_0 = \phi - \omega(I)$ . We require an absolute error smaller than  $10^{-5}$  in the fixed point to stop the iteration. There is no point in requiring higher precision, because the error of our series representation in the angle variable is larger than  $10^{-2}$ ; see Table 4 (bottom panel).

Once  $\phi'$  is known,  $I'$  is obtained directly from Equation (9b).

## 5. Approximation Error

Now we have two different representations of the scattering map:

- The **numerical scattering map**  $\sigma(I, \phi)$  was obtained in Section 3 using normal forms and numerical continuation of the invariant manifolds. It was calculated on a relatively coarse grid of points (Figure 9).
- The **scattering map series**  $\tilde{\sigma}(I, \phi)$  consists in the Fourier-Taylor approximation (10)-(11) and (15). The series approximation has been derived from the numerical map in Section 4, so it is not as precise. However, it has the advantage that it can be evaluated at any desired point  $(I, \phi)$ .

To measure the quality of the series approximation, we do the following:

1. Read the numerical scattering map from file as a table:

$$(I', \phi') = \sigma(I, \phi).$$

We only have its values on a coarse grid of points  $(I, \phi)$ .

2. Compute the scattering map series *on the same grid*:

$$(\tilde{I}', \tilde{\phi}') = \tilde{\sigma}(I, \phi).$$

3. Find the approximation error, defined as the *maximum over all grid points* of

$$(\epsilon_I, \epsilon_\phi) = \left( \left| \tilde{I}' - I' \right|, \left| \tilde{\phi}' - \phi' \right| \right).$$

Of course, the approximation error depends on the chosen degree  $(N, L)$  of the Fourier-Taylor approximation. For illustration, Figures 13 and 14 compare the quality of a low order versus a high order approximation.

We will distinguish two different settings. In the *local* setting, one is interested in an accurate representation of the scattering map in a neighborhood of  $I = 0$ , whereas in the *global* setting, one is interested in an accurate representation in the whole domain of the global scattering map.

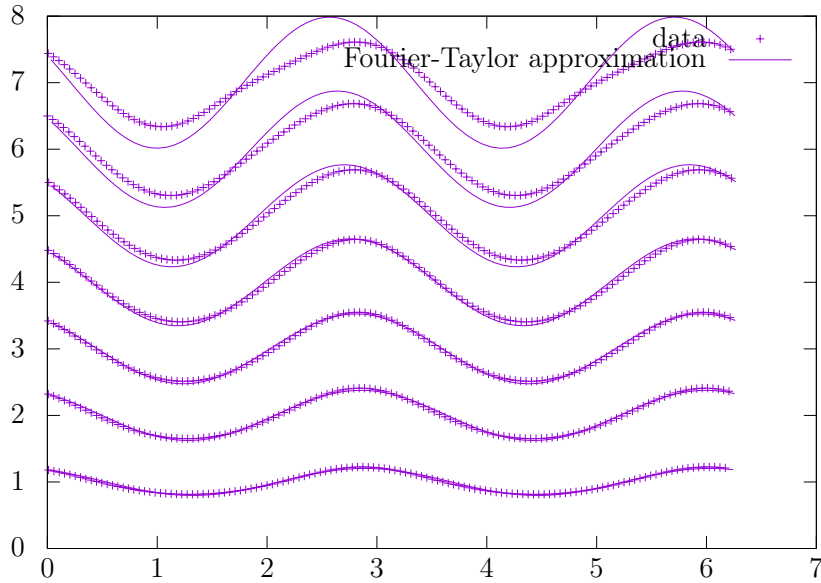


Figure 13: Image of the numerical scattering map (points) versus the scattering map series of degree  $N = 2, L = 2$  (lines).

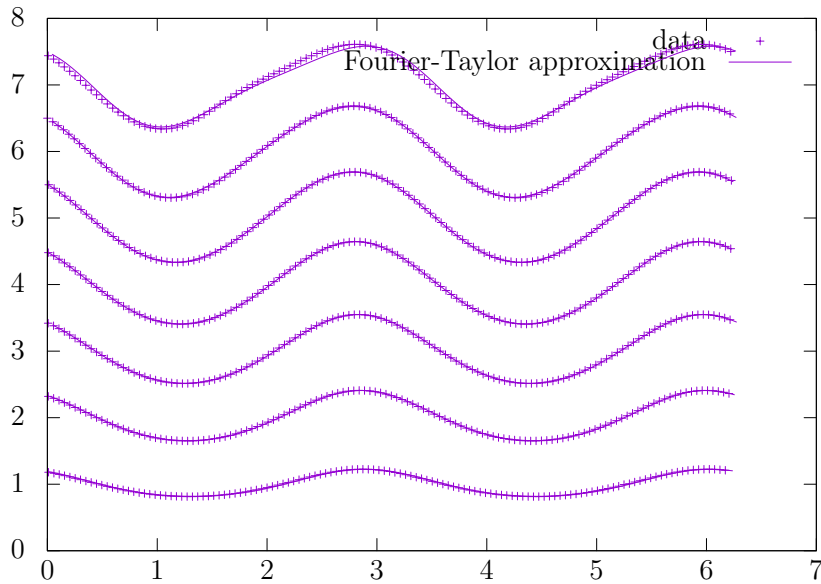


Figure 14: Image of the numerical scattering map (points) versus the scattering map series of degree  $N = 4, L = 5$  (lines).

L				
N	0	1	2	3
2	0.540000	0.134772	0.041698	0.037342
4	0.540000	0.145286	0.019337	0.011640
6	0.540000	0.151078	0.019536	0.013382

L			
N	0	1	2
2	0.156427	0.052403	0.015123
4	0.156427	0.049706	0.016311
6	0.156427	0.049634	0.016270

Table 3: Local approximation error  $\epsilon_I$  (top panel) and  $\epsilon_\phi$  (bottom panel) as a function of  $N, L$  for the first scattering map  $\sigma_1$ .

### 5.1. Local Approximation Error

For definiteness, let's fix the local domain to be

$$\mathcal{A}_{\text{loc}} = \{(I, \phi) : I \in (0, 3] \text{ and } \phi \in [0, 2\pi)\}.$$

We have computed the approximation error over the local domain  $\mathcal{A}_{\text{loc}}$  as a function of the degree  $(N, L)$  of the Fourier-Taylor expansion; see Table 3.

*Remark 17.* Only the grid points  $(I, \phi)$  belonging to the local domain (i.e. tori  $I = 1, 2, 3$ ) are used in the computation of the local approximation error.

The error of the Fourier-Taylor model decreases as  $N$  and  $L$  increase, but not monotonically. If we want an approximation error  $\epsilon = \max\{\epsilon_I, \epsilon_\phi\}$  less than 0.05, then it is enough to take  $N = 2$  and  $L = 2$ . Notice that the improvement is mild beyond that point. Indeed, Figure 13 shows that  $N = L = 2$  gives a good approximation in the local domain  $\mathcal{A}_{\text{loc}}$ .

Thus, it is natural to choose  $N = L = 2$  to obtain an accurate model for the local scattering map. In fact, as discussed before (Remark 13), we neglect the odd Fourier coefficients  $A_1(I)$  and  $B_1(I)$  due to the symmetry of the problem, and just keep the even ones  $A_2(I)$  and  $B_2(I)$ .

Therefore, in the local setting, an **accurate model** for the scattering map is given by the Fourier-Taylor expansion

$$\tilde{\mathcal{L}}(I, \phi') = -\frac{B_2(I)}{2} \cos 2\phi' + \frac{A_2(I)}{2} \sin 2\phi',$$

		L						
N	0	1	2	3	4	5	6	7
2	0.680000	0.963414	0.495653	0.261042	0.385496	0.131751	0.219163	0.094550
4	0.680000	0.975219	0.618115	0.276085	0.387552	0.087317	0.156552	0.021123
6	0.680000	0.996139	0.656461	0.266668	0.381078	0.107612	0.144998	0.013382
8	0.680000	1.003501	0.657922	0.287596	0.367730	0.110813	0.148937	0.013159
10	0.680000	1.007927	0.647908	0.287781	0.356098	0.105846	0.149545	0.012512

		L					
N	0	1	2	3	4	5	6
2	0.449508	0.268271	0.157380	0.065119	0.148788	0.068206	0.121809
4	0.449508	0.270152	0.169874	0.074112	0.150692	0.085074	0.132709
6	0.449508	0.269731	0.169564	0.076822	0.153570	0.083003	0.132714
8	0.449508	0.269683	0.169068	0.079125	0.155540	0.083914	0.131502
10	0.449508	0.269748	0.169407	0.080213	0.157050	0.085329	0.131450

Table 4: Global approximation error  $\epsilon_I$  (top panel) and  $\epsilon_\phi$  (bottom panel) as a function of  $N, L$  for the first scattering map  $\sigma_1$ .

where

$$\begin{aligned}
A_2(I) &= \tilde{a}_0^{(2)} + \tilde{a}_1^{(2)}I + \tilde{a}_2^{(2)}I(I-1) \\
B_2(I) &= \tilde{b}_0^{(2)} + \tilde{b}_1^{(2)}I + \tilde{b}_2^{(2)}I(I-1), \\
\omega(I) &= \tilde{c}_0 + \tilde{c}_1(I-1) + \tilde{c}_2(I-1)(I-2),
\end{aligned}$$

consisting of only nine coefficients. These coefficients were given in Tables 1 and 2.

### 5.2. Global Approximation Error

Suppose now that we are now interested in an accurate representation in the whole domain of the scattering map

$$\mathcal{A} = \{(I, \phi) : I \in (0, 7] \text{ and } \phi \in [0, 2\pi)\}. \quad (16)$$

The approximation error over the global domain is given in Table 4. If we want an approximation error  $\epsilon = \max\{\epsilon_I, \epsilon_\phi\}$  less than 0.1, we need to increase the degree of the Fourier-Taylor series to  $N = 4$  and  $L = 5$ . Indeed, Figure 14 shows that  $N = 4, L = 5$  gives a good approximation in the global domain  $\mathcal{A}$ .

From now on, we will use  $N = 4$ ,  $L = 5$  as our model for the global scattering map  $\sigma_1$ .

A similar analysis suggests to use  $N = 4$ ,  $L = 6$  for the global scattering map  $\sigma_2$ .

## 6. Inner Map

Recall that the *inner flow* refers to the restriction of the RTBP flow to the normally hyperbolic invariant manifold  $\Lambda_c$ , while the *inner map* refers to the restriction of the first return map  $\mathcal{F}$  to  $\Lambda_c$ . Abusing notation, the inner map will still be called  $\mathcal{F}$ .

As explained in Section 2.1, the RTBP flow on the center manifold  $W^c(L_1)$  consists simply on a translation on the 2-torus,

$$\begin{aligned} \dot{J}_p &= 0, & \dot{\phi}_p &= \frac{\partial H}{\partial J_p} =: \nu_p(J_p, J_v), \\ \dot{J}_v &= 0, & \dot{\phi}_v &= \frac{\partial H}{\partial J_v} =: \nu_v(J_p, J_v). \end{aligned}$$

The value of the planar and vertical frequencies  $\nu_p$ ,  $\nu_v$  of the torus are obtained differentiating the Hamiltonian in normal form.

Upon restriction to the NHIM  $\Lambda_c$ , we get rid of the planar action  $J_p$ , which can be recovered if necessary using the energy condition, so the inner flow is

$$\dot{J}_v = 0, \quad \dot{\phi}_p = \nu_p(J_v), \quad \dot{\phi}_v = \nu_v(J_v). \quad (17)$$

Finally, the first return map of the inner flow to the section  $\Sigma$  is

$$J'_v = J_v, \quad \phi'_v = \phi_v + \frac{2\pi\nu_v(J_v)}{\nu_p(J_v)}.$$

In terms of the scaled coordinates  $I, \phi$ , the inner map  $\mathcal{F}: \Lambda_c^\Sigma \rightarrow \Lambda_c^\Sigma$  is given by

$$I' = I, \quad \phi' = \phi + \nu(I), \quad (18)$$

where we have introduced the new function

$$\nu(I) := \frac{2\pi\nu_v(I/1000)}{\nu_p(I/1000)}.$$

As seen in Figure 15, the inner shift  $\nu(I)$  decreases almost linearly with  $I$ . In particular, this shows that the inner map  $\mathcal{F}$  is a twist map.

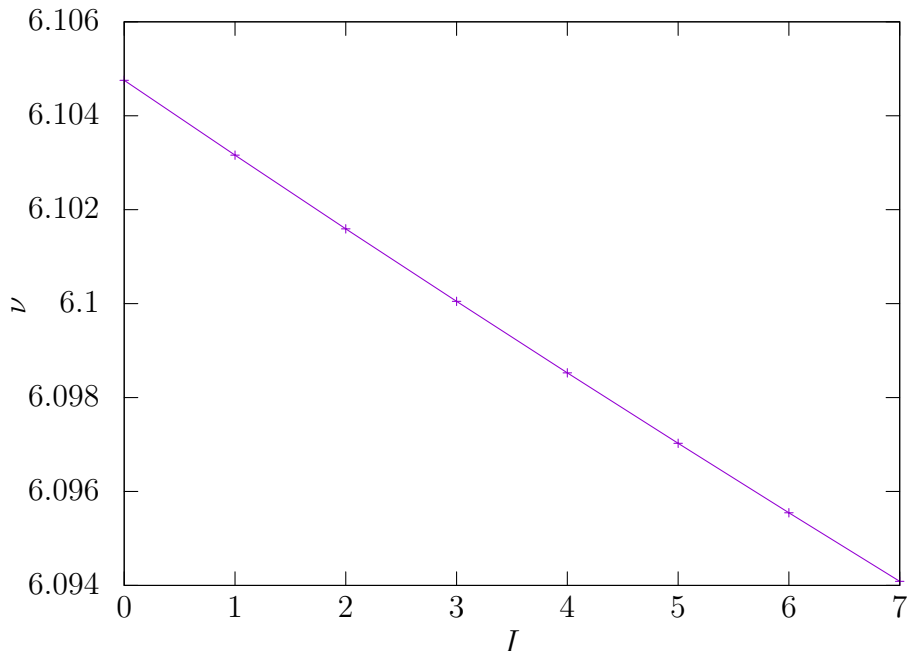


Figure 15: The inner shift  $\nu(I)$ .

## 7. Phase Space of the Scattering Map

In Sections 4 and 5, we have obtained a series representation of the scattering maps  $\sigma(I, \phi)$  with small approximation error. This representation is valid on an annulus  $\mathcal{A}$  inside the NHIM (see Equation (16)). Thus we can now iterate the scattering map in  $\mathcal{A}$ .

To explore the global phase space of the scattering map, we perform the following experiment: take 100 initial conditions equi-distributed on the line  $\{I \in [0, 7], \phi = 0\}$ , and iterate each initial condition 1000 times by the scattering map. The resulting phase space portrait is shown in Figure 16.

Notice that the scattering map (9), rewritten as

$$\phi' = \phi - \omega(I) - \frac{\partial \tilde{\mathcal{L}}}{\partial I}(I, \phi') \quad (19a)$$

$$I' = I + \frac{\partial \tilde{\mathcal{L}}}{\partial \phi'}(I, \phi') \quad (19b)$$

can be seen as a perturbation of the integrable map  $(I, \phi) \mapsto (I' = I, \phi' = \phi - \omega(I))$ , as long as the derivatives of  $\tilde{\mathcal{L}}$  are small enough. The frequency  $-\omega(I)$  represents the *phase shift* of the map  $(I, \phi) \mapsto (I' = I, \phi' = \phi - \omega(I))$ .

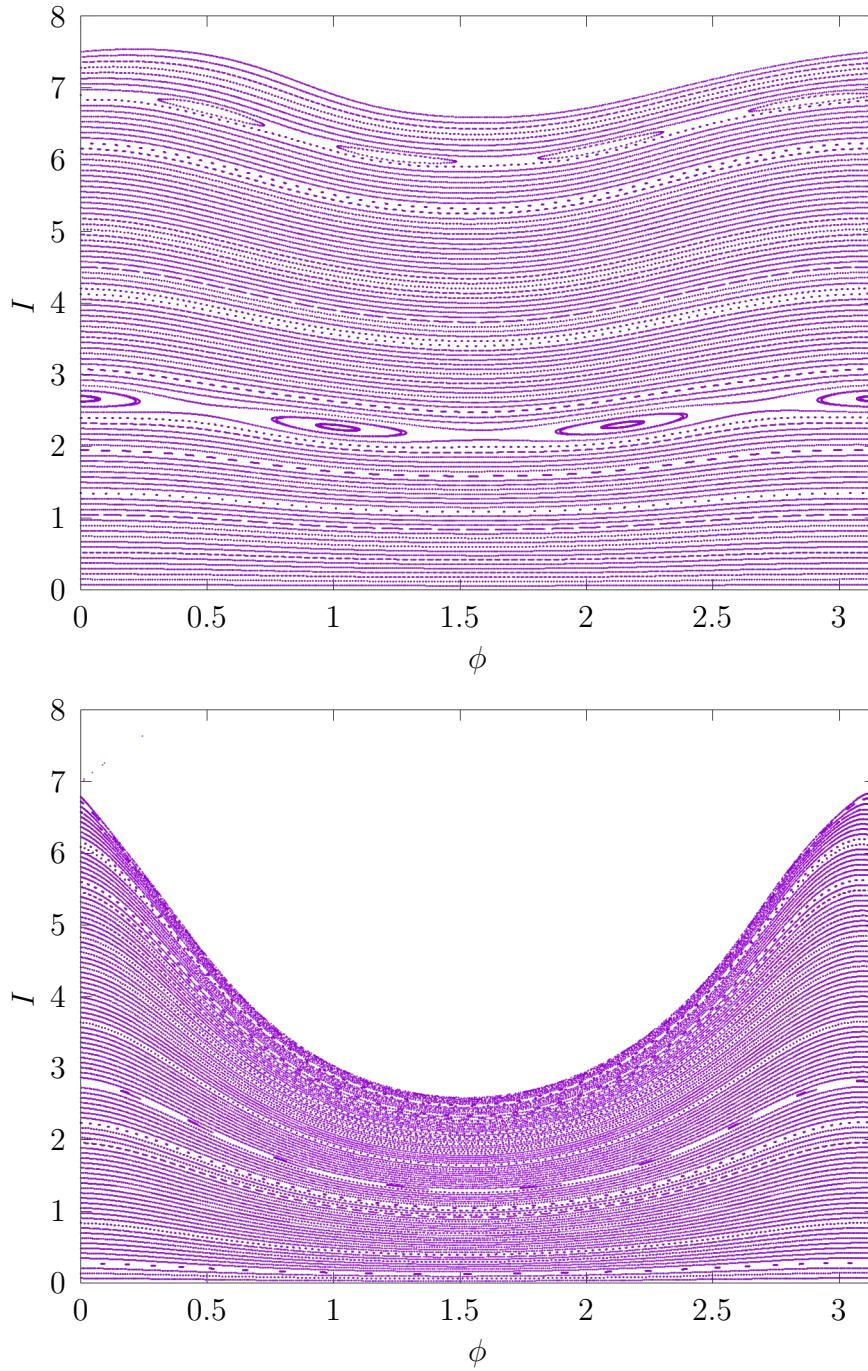


Figure 16: Phase portrait of the scattering maps  $\sigma_1$  (above) and  $\sigma_2$  (below).



Since  $\omega'(I) \neq 0$  (see Figure 12), the integrable map  $(I, \phi) \mapsto (I, \phi - \omega(I))$  is a twist map. Below we check that the scattering map is also a twist map. (See ‘Twist Condition’).

By KAM theory (for an area preserving map given by its generating function; see, for instance, [45, 46]), when the derivatives of  $\tilde{\mathcal{L}}$  are small, we expect that many of the invariant tori of the integrable twist map persist.

### Phase Shift

The phase shift of the scattering map (19) is  $\phi' - \phi = -\omega(I) - \frac{\partial \tilde{\mathcal{L}}}{\partial I}(I, \phi')$ . The divided differences of  $\omega(I)$  are listed in Table 2. From these data we see that  $|\tilde{c}_0| \gg |\tilde{c}_1| \gg |\tilde{c}_j|$  for  $j = 2, \dots, 6$ . Comparing with Table 1, we notice that  $|\tilde{c}_0| \gg |\tilde{a}_j^n|, |\tilde{b}_j^n|$ ,  $j = 1, \dots, 7$ ,  $n = 2, 4, 6, 8$ . This implies that  $\frac{\partial \tilde{\mathcal{L}}}{\partial I}$  is much smaller than  $\omega(I)$ , which is non-zero, at least for  $I$  small enough. This argument could be used to assert that the phase shift is non-zero in the local domain  $\mathcal{A}_{\text{loc}}$ .

To deal with the global domain  $\mathcal{A}$ , we determine the range of  $I$  values where the phase shift is non-zero. The phase shift is bounded by

$$-\omega(I) - \max_{\phi'} \left| \frac{\partial \tilde{\mathcal{L}}}{\partial I}(I, \phi') \right| \leq -\omega(I) - \frac{\partial \tilde{\mathcal{L}}}{\partial I}(I, \phi') \leq -\omega(I) + \max_{\phi'} \left| \frac{\partial \tilde{\mathcal{L}}}{\partial I}(I, \phi') \right|.$$

We have computed these bounds explicitly, using the series expansions of  $\omega(I)$  and  $\frac{\partial \tilde{\mathcal{L}}}{\partial I}(I, \phi')$ . The result is shown in Figure 17. Note that the phase shift for  $\sigma_1$  is non-zero for all  $I \in (0, 7]$ , while the phase shift for  $\sigma_2$  (modulo  $\pi$ ) is non-zero except possibly for a small range of  $I$  values close to  $I = 7$ .

### Twist Condition

Let us compute the twist of the scattering map (19):

$$\frac{\partial \phi'}{\partial I}(I, \phi') = -\omega'(I) - \frac{\partial^2 \tilde{\mathcal{L}}}{\partial I^2}(I, \phi') - \frac{\partial^2 \tilde{\mathcal{L}}}{\partial \phi' \partial I}(I, \phi') \frac{\partial \phi'}{\partial I}.$$

Thus

$$\frac{\partial \phi'}{\partial I}(I, \phi') = -\frac{\omega'(I) + \frac{\partial^2 \tilde{\mathcal{L}}}{\partial I^2}}{1 + \frac{\partial^2 \tilde{\mathcal{L}}}{\partial \phi' \partial I}}, \quad (20)$$

provided that the denominator is non-zero.

We have computed the twist (20) explicitly on the global domain  $\mathcal{A}$ , using the series expansions of  $\omega(I)$  and  $\tilde{\mathcal{L}}(I, \phi')$ . The result is shown in Figure 18. Note that the twist for both  $\sigma_1$  and  $\sigma_2$  is non-zero in  $\mathcal{A}$ .

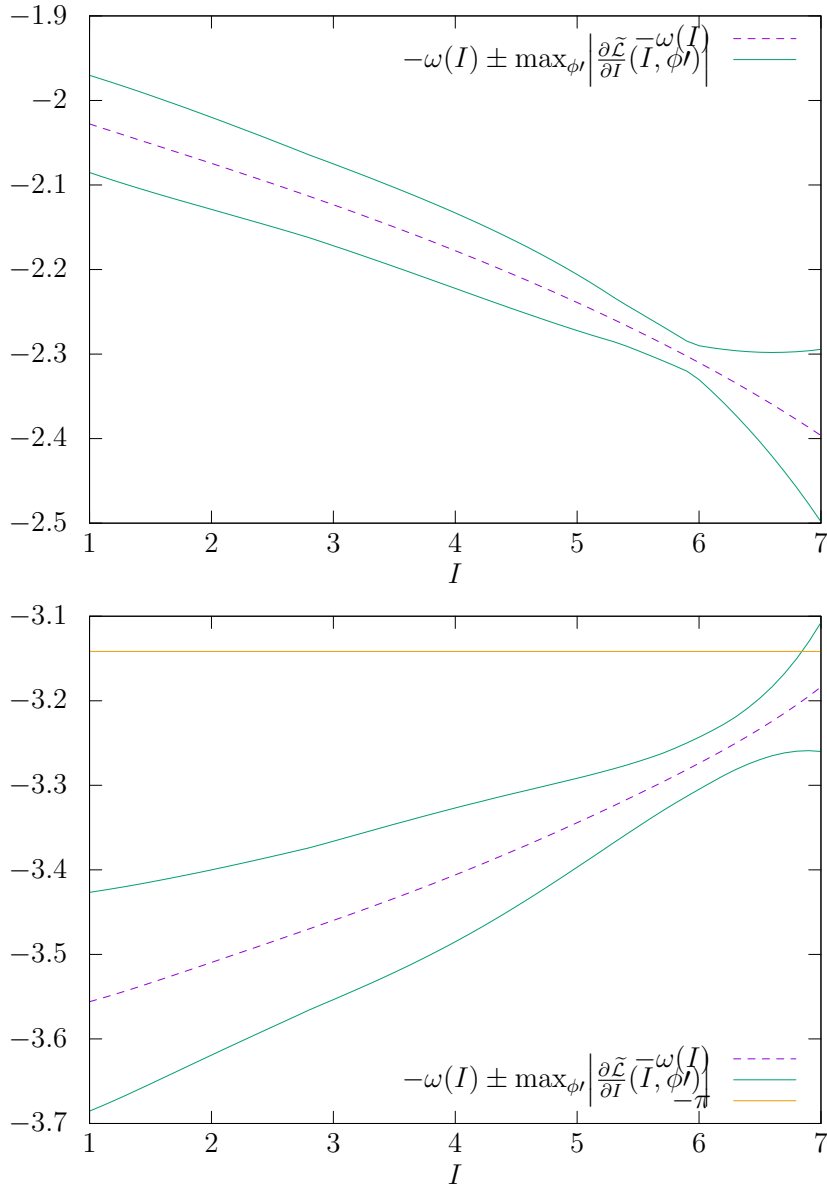


Figure 17: Enclosure of the phase shift for the scattering map  $\sigma_1$  (above) and  $\sigma_2$  (below). The phase shift  $-\omega(I) - \frac{\partial \tilde{\mathcal{L}}}{\partial I}(I, \phi')$  is enclosed inside the green lines.

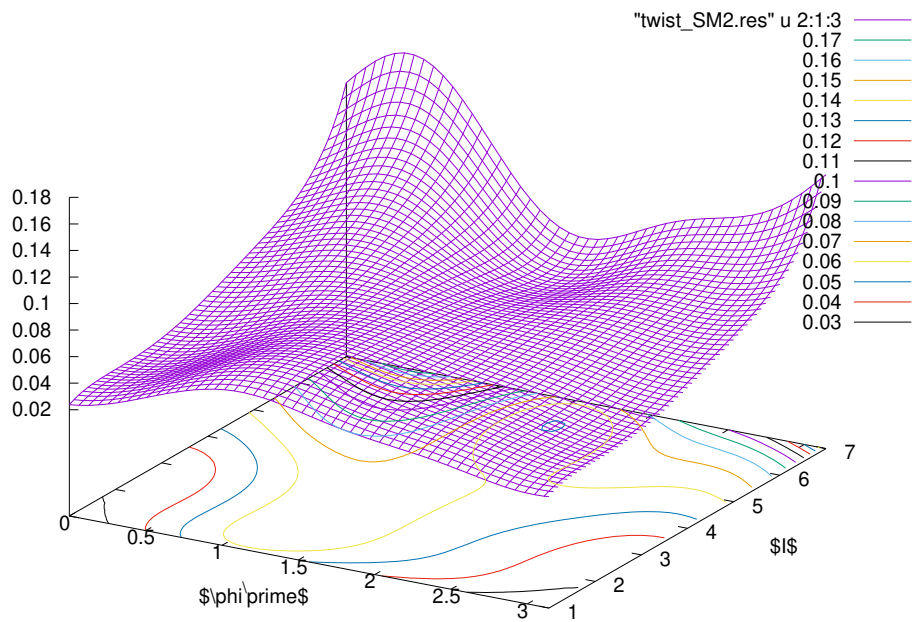
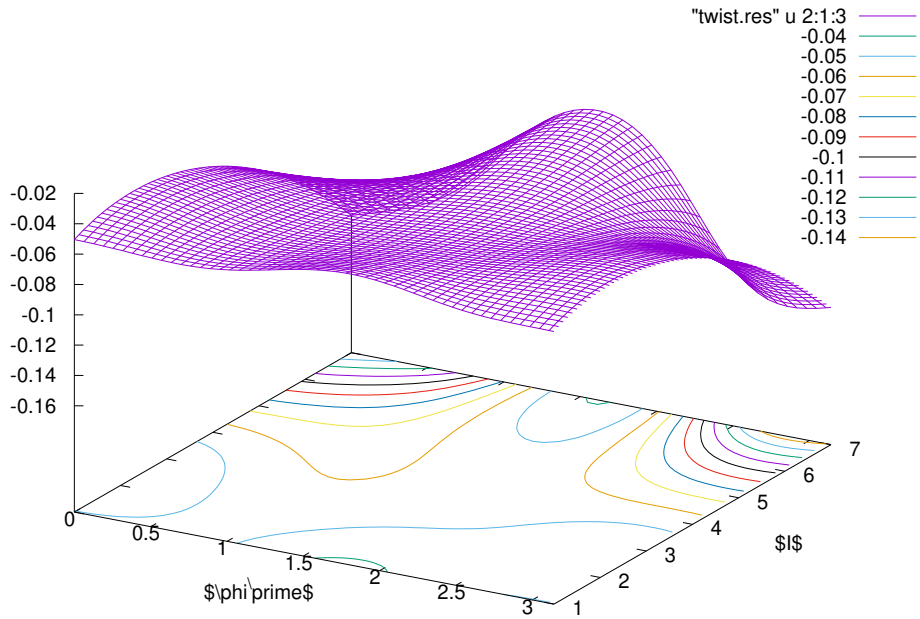


Figure 18: Twist for the scattering map  $\sigma_1$  (above) and  $\sigma_2$  (below).

## 8. KAM tori and resonant zones for the Scattering Maps

As seen in Figure 16, the phase portrait of the scattering maps  $\sigma_1, \sigma_2$  is filled up with invariant curves and some resonant zones between them. Recall from Section 7 that both  $\sigma_1$  and  $\sigma_2$  are twist maps. To compute these invariant curves, we now introduce the exponential form in the sine-cosine Fourier expansion (12) of  $\frac{\partial \tilde{\mathcal{L}}}{\partial \phi'}$

$$\frac{\partial \tilde{\mathcal{L}}}{\partial \phi'} = \sum_{n=1}^N A_n \cos n\phi' + \sum_{n=1}^N B_n \sin n\phi' = \sum_{n=-N, n \neq 0}^N C_n e^{in\phi'},$$

where  $C = (C_{-N}, \dots, C_{-1}, C_1, \dots, C_N) \in \mathbb{C}^{2N}$  satisfies

$$C_n = \frac{1}{2}(A_n - iB_n), \quad C_{-n} = \frac{1}{2}(A_n + iB_n) = \overline{C_n}, \quad \text{for } n > 0.$$

Notice that for  $\tilde{\mathcal{L}} = 0$ , or equivalently  $C = 0$ , any torus  $I = I_0$  is invariant since then  $I' = I_0$  in the expression (19b) of a scattering map, with an inner dynamics  $\phi' = \phi - \omega_0$  given by (19a), where  $\omega_0 := \omega(I_0)$ .

For  $|\tilde{\mathcal{L}}|$  small enough, or equivalently  $|C|$  small enough, a lot of these invariant curves survive. An invariant curve  $I = I_0 + h(\phi)$  of a scattering map (19) satisfies  $I' = I_0 + h(\phi')$ , that is

$$h(\phi') = h \left( \phi' + \omega(I) + \frac{\partial \tilde{\mathcal{L}}}{\partial I}(I, \phi') \right) + \frac{\partial \tilde{\mathcal{L}}}{\partial \phi'}(I, \phi'), \quad \text{where } I = I_0 + h(\phi).$$

Expanding in  $C$  and  $h$  we get

$$h(\phi') = h(\phi' + \omega_0) + \frac{\partial \tilde{\mathcal{L}}}{\partial \phi'}(I, \phi') + O(hC).$$

Writing  $h(\phi') = \sum_{n=-N, n \neq 0}^N h_n e^{in\phi'}$  we get

$$\sum h_n e^{in\phi'} = \sum e^{in\omega_0} h_n e^{in\phi'} + \sum C_n e^{in\phi'} + O(hC),$$

which, equating Fourier coefficients, gives

$$h_n = -\frac{C_n}{e^{in\omega_0} - 1} + O(C^2) \quad \text{for } 0 < |n| \leq N.$$

For this approximate formula one needs that  $\frac{n\omega_0}{2\pi} \notin \mathbb{Z}$  for  $|n| \leq N$  (non-resonant condition), and one sees that, up to order  $O(C^2)$ , the coefficients  $h_n = O(C)$  are uniquely determined by  $C$ . KAM theorem consists in proving the convergence of these expansions for *diophantine frequencies*  $\omega_0$ , using that  $\sigma_1$  and  $\sigma_2$  are twist maps.

### *Resonant Zones for $\sigma_1$*

Resonant zones for the symplectic map (9), or, equivalently, (19), where the KAM theorem does not provide invariant curves for small  $\mathcal{L}$ , appear around the values  $I$  such that  $\frac{\omega(I)}{\pi}$  is a rational number. In the global setting,

$$\omega(I) = \Omega'(I) \approx \sum_{l=0}^L c_l N_l(I),$$

where the coefficients  $c_l$  are given in table 2 for both scattering maps  $\sigma_1$  and  $\sigma_2$ .

In particular for  $\sigma_1$  (a totally analogous study for  $\sigma_2$  can be carried out)  $\frac{\omega(0)}{\pi} = 0.630128\dots$ , which is not too far for  $2/3$  whose continued fraction is  $[1,2]$ , which means that

$$\frac{2}{3} = [1, 2] = \frac{1}{1 + \frac{1}{2}}.$$

Therefore for  $I$  such that  $\frac{\omega(I)}{\pi} = \frac{2}{3}$ , which happens to be  $I \approx 2.4175$ , there should appear a resonance, indeed the largest one, since the width of the ‘eyes’ of a resonance is related to the denominator, in this case 3.

Other close rationals to  $2/3$  are given by close modified continued fractions. For instance

$$[1, 2, 1] = \frac{1}{1 + \frac{1}{2 + \frac{1}{1}}} = \frac{3}{4}.$$

We can compute some of the largest ones, ordered by their denominators:

$I$	$\frac{\omega(I)}{\pi}$	continued fraction
2.4175	$\frac{2}{3}$	[1,2]
6.5550	$\frac{3}{4}$	[1,2,1]
5.0752	$\frac{5}{7}$	[1,2,2]
4.3631	$\frac{7}{10}$	[1,2,3]
3.9523	$\frac{9}{13}$	[1,2,4]

The continued fraction of  $\frac{2}{3}$  can be also written as [1,1,1], and smaller resonant values can be obtained for smaller continued fractions like  $[1, 1, 1, 3] = \frac{7}{11} = 0.636363\dots$ , etc

For the scattering map  $\sigma_1$ , the two main resonances are clearly visible near  $I \approx 2.4175$  and  $I \approx 6.5550$ . See Figure 16 (top panel).

## 9. Heuristic argument for Arnold diffusion

The Hamiltonian that describes the normal form is integrable, and, in particular,  $\Lambda_c^\Sigma$  is foliated by circles invariant under  $\mathcal{F}$ . That is, the inner map  $\mathcal{F}$  preserves each level set of  $I$  in  $\Lambda_c^\Sigma$ . However, by combining the inner dynamics restricted to  $\Lambda_c^\Sigma$  with the outer dynamics along homoclinic trajectories we can obtain drift trajectories along which  $I$  changes significantly, thus exhibiting Arnold diffusion. In this section we provide a heuristic argument for Arnold diffusion in the variable  $I$ .

Our argument is based on a result from [47], which was subsequently extended in [48] and [30]. Let  $\mathbb{A} = [0, 1] \times \mathbb{T}$  be a two-dimensional annulus, where  $\mathbb{T} = \mathbb{R}/\mathbb{Z}$ , and  $(I, \phi) \in [0, 1] \times \mathbb{T}$  be coordinates on  $\mathbb{A}$ .

**Theorem 1** ([47]). *Let  $f, g : \mathbb{A} \rightarrow \mathbb{A}$  be two  $C^1$ -diffeomorphisms of the annulus that preserve the boundary circles.*

*Assume the following*

- (i)  $f$  is a twist map;
- (ii)  $g$  is an area preserving map;
- (iii) Every essential invariant circle  $\Gamma$  for  $f$  is not invariant under  $g$  (we recall that an essential circle for  $f$  is a simple closed  $C^0$ -curve in  $\mathbb{A}$  that is nonhomotopic to zero).

Then, for every pair of open neighborhoods  $U_0$  of  $\mathbb{T} \times \{0\}$  and  $U_1$  of  $\mathbb{T} \times \{1\}$  in  $\mathbb{A}$ , there exists an orbit  $(z_n)_{n=0, \dots, N}$  of the IFS generated by  $\{f, g\}$  such that  $z_0 \in U_0$  and  $z_1 \in U_1$ ; the orbit if the iterated function system (IFS) is defined at every step by a choice  $z_{n+1} = f(z_n)$  or  $z_{n+1} = g(z_n)$ .

As the orbits of the IFS are not true orbits of the system, we refer to them as pseudo-orbits.

To apply Theorem 1 we let

$$\mathbb{A} = \{(I, \phi) \mid I \in [1, 7], \phi \in [0, 2\pi)\}$$

be the annulus where we want to show diffusion,  $f$  be the inner map  $\mathcal{F}$  restricted to  $\mathbb{A}$ , and  $g$  be either  $\sigma_1$  or  $\sigma_2$ . Recall that  $\mathcal{F}$  is a twist map. In Section 7 we verified numerically that  $\sigma_1$  and  $\sigma_2$  are twist maps as well.

As seen in Table 1, the harmonics of  $\tilde{\mathcal{L}}$  for both scattering maps  $\sigma_1$  and  $\sigma_2$ , particularly those of degree two, are not zero, so that the inner map and any of these scattering maps can not have common invariant curves, and by Theorem 1 both the double dynamical systems  $\{\mathcal{F}, \sigma_1\}$  and  $\{\mathcal{F}, \sigma_2\}$  formed by the inner map and one of the scattering maps have diffusing pseudo-orbits along the NHIM.

Even more, for the two scattering maps described in Table 1, one sees that the difference between the respective coefficients  $C_n$  is greater than 0.04 for the coefficients  $C_{\pm 1}$  due to  $\tilde{a}_1$ . This, together with the fact that the magnitude of the denominator  $e^{\pm i\omega_0} - 1$  in the formula of  $h_{\pm 1}$  is much smaller than 1, prevents the two scattering maps from having common invariant curves, which, on the other hand, is clearly observed in the juxtaposition of the curves found numerically for the two scattering maps. This implies that the double dynamical system  $\{\sigma_1, \sigma_2\}$  also has diffusing orbits along the NHIM.

We can take advantage of these dynamics to construct fast diffusing pseudo-orbits obtained from the triple dynamical system  $\{\mathcal{F}, \sigma_1, \sigma_2\}$  formed by the inner map and the two scattering maps. We will give explicit constructions of diffusing (pseudo-)orbits, including fast ones, in Section 11.

Once such pseudo-orbits are obtained, the shadowing lemma [49, Theorem 3.7] gives true orbits that shadow the pseudo-orbits, thus achieving Arnold diffusion.

Note that the above construction of diffusing (pseudo-)orbits assumes that the inner dynamics is derived from the normal form approximation, which is given by an integrable Hamiltonian. However, the original Hamiltonian is not

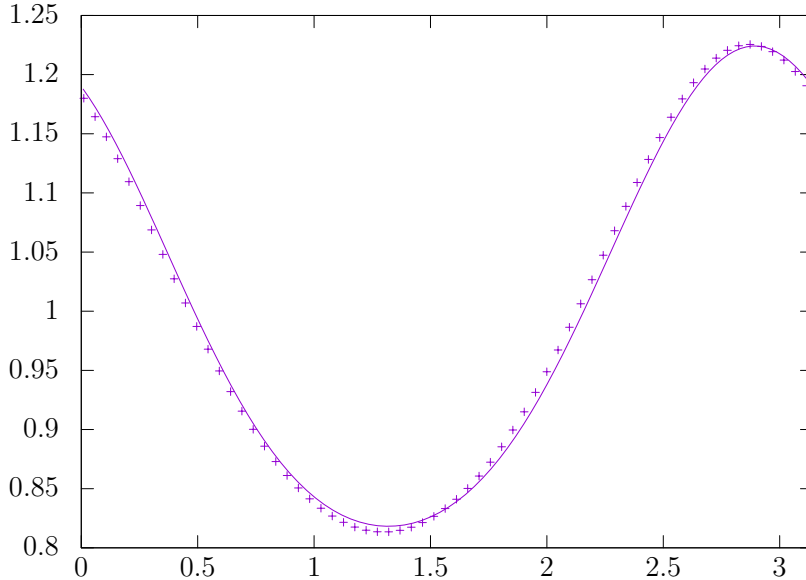


Figure 19: Image of the action level  $I = 1$  by the numerical scattering map (points) versus the scattering map series  $N = 4, M = 5$  (lines).

integrable, and the NHIM  $\tilde{\Lambda}_c^\Sigma$  for the original Hamiltonian is not foliated by circles invariant under the true inner map. We will now argue the existence of diffusing orbits for the original system. Let  $f = \tilde{\mathcal{F}}$  be the inner map restricted to the NHIM  $\tilde{\Lambda}_c^\Sigma$  for the original Hamiltonian, and let  $g$  be either  $\sigma_1$  or  $\sigma_2$ .

Recall that the inner map for the normal form is an integrable twist map, and the global error in the numerical integration of orbits with initial condition  $(J, \phi_p, \phi_v)$  is less than  $10^{-12}/5000$ ; see Section 3. (We recall  $J = J_v$  is the vertical amplitude of the motion.) Since each level set of  $J$  is preserved by the inner dynamics  $\mathcal{F}$  for the normal form, and since  $I = 1000J$ , it follows that each essential invariant circle  $\Gamma$  for the inner map  $\tilde{\mathcal{F}}$  for the original Hamiltonian is less than  $10^{-9}/1500$  away from a level set of  $I$ .

We also know from Section 3.2 that the scattering maps  $\sigma_1, \sigma_2$  are globally defined on  $\mathbb{A}$ . Moreover, for each  $I$  in the interval  $[1, 7]$ , the oscillation

$$\sup_{\phi} \sigma_1(I, \phi) - \inf_{\phi} \sigma_1(I, \phi)$$

of  $\sigma_1$  is bigger than 0.2.

To see this, note that the smallest oscillations in Figure 14 happen for the



action level  $I = 1$ . Zooming in that action level (Figure 19), it is clear that the oscillation is bigger than 0.2, say. Alternatively, approximate the image of  $I = 1$  by the truncated Fourier-Taylor series consisting of the dominant coefficients

$$I' = I + \tilde{a}_1^{(2)} \cos 2\phi' + \tilde{b}_1^{(2)} \sin 2\phi',$$

where  $\tilde{a}_1^{(2)} = 0.178180$  and  $\tilde{b}_1^{(2)} = -0.097275$  (See Table 1). This function has oscillations of size twice its amplitude  $\sqrt{\left(\tilde{a}_1^{(2)}\right)^2 + \left(\tilde{b}_1^{(2)}\right)^2} = 0.203003$ .

Similarly, the oscillation of  $\sigma_2$  is bigger than 0.3.

These facts imply that no essential invariant circle  $\Gamma$  for  $\tilde{\mathcal{F}}$  is invariant under  $\sigma_1$  or  $\sigma_2$ . Therefore, Theorem 1 applies and there are orbits of the IFS  $\{\tilde{\mathcal{F}}, \sigma_1\}$ , as well as orbits of the IFS  $\{\tilde{\mathcal{F}}, \sigma_2\}$ , that go from the lower boundary of the annulus  $\mathbb{T} \times \{0\}$  to its upper boundary.

Again, the shadowing lemma [49, Theorem 3.7] gives true orbits that shadow the obtained pseudo-orbits, thus achieving Arnold diffusion.

## 10. Time Estimates for Inner and Transition Map

One of our main goals is to estimate the drift time spent by drift orbits, constructed in Section 11. As an intermediate step, we measure the time spent on one iterate of the inner map ('inner time', or  $t_{\text{in}}$ ), and the time spent on one iterate of the transition map ('outer time', or  $t_{\text{out}}$ ).

In terms of the RTBP inner flow (17), one application of the inner map corresponds to integrating an initial condition  $(J_v, \phi_p = 0, \phi_v) \in \Lambda_c^\Sigma$  during the amount of time that it takes to return to the section  $\Sigma$ . Thus, each iterate of the inner map takes time

$$t_{\text{in}} = \frac{2\pi}{\nu_p}.$$

Numerically, we find that  $2.0764 < \nu_p(I) < 2.0781$ , and therefore the inner time is bounded by

$$3.0235 < t_{\text{in}} < 3.0261.$$

In terms of the RTBP flow, one application of the transition map corresponds to a (segment of) a homoclinic trajectory from  $y_- \in W_{\text{loc}}^u(\Lambda_c)$  to  $y_+ \in W_{\text{loc}}^s(\Lambda_c)$ . As noted in Section 3, the flight time of homoclinic segments is bounded by

$$5.936738 \leq t_{\text{out}} \leq 6.000688.$$

Therefore in our setting we find that outer times  $t_{\text{out}}$  are approximately twice as long as inner times  $t_{\text{in}}$ .

## 11. Drift Orbits

In the previous section we provided some heuristic arguments for the existence of trajectories that undergo Arnold diffusion in the sense that they drift in terms of the scaled out-of-plane amplitude  $I$  (see (8)). Our arguments only show that such drift orbits exist, but do not provide a way to find them. Moreover, they do not provide methods to find orbits that drift ‘fast’.

In this section, we propose different algorithms to produce drift orbits, i.e., orbits of the iterated function system (IFS) consisting of the inner and outer map, whose action variable  $I$  increases from  $I = 1$  to  $I > 7$ . We produce two different type of orbits:

- Orbits of the iterated function system  $\{\mathcal{F}, \sigma_1\}$ ,  $\{\mathcal{F}, \sigma_2\}$ , or  $\{\mathcal{F}, \sigma_1, \sigma_2\}$ . These orbits are a realization of the existence Theorem 1. We look for short orbits, i.e. we try to minimize the number of iterates. However, it is important to realize that **these orbits do not directly translate to pseudo-orbits for the R3BP flow**. The reason is that the scattering map is not dynamically defined; it is geometrically defined instead (i.e. one iterate of the scattering map does not correspond to a segment of homoclinic trajectory).
- Orbits of the iterated function system  $\{\mathcal{F}, \tau_1\}$ ,  $\{\mathcal{F}, \tau_2\}$ , or  $\{\mathcal{F}, \tau_1, \tau_2\}$ . These are also a realization of the existence Theorem 1, and they **directly translate to pseudo-orbits of the R3BP flow**. Each iterate of the transition map corresponds to a segment of homoclinic trajectory. Using the time estimates of Section 10, we can estimate the total drift time of the pseudo-orbit as:

$$t = n_0 t_{\text{in}} + n_1 t_{\text{out}} + n_2 t_{\text{out}},$$

where  $n_0$ ,  $n_1$  and  $n_2$  denote the number of iterates of  $\mathcal{F}$ ,  $\tau_1$  and  $\tau_2$  respectively. Keeping an eye on Astrodynamics applications, we want to minimize the total drift time.

11.1. *Double Dynamical System  $\{\mathcal{F}, \sigma_i\}$ . Greedy Algorithm.*

In Section 8 we already established that  $\sigma_i$  ( $i = 1, 2$ ) has many invariant curves. All iterates of  $\sigma_i$  either belong to an invariant curve, or are confined between two invariant curves. Thus it is not possible to cross from  $I = 1$  to  $I > 7$  using just one scattering map  $\sigma_i$ .

However, according to Theorem 1, one can combine the inner and outer map to produce drift orbits. Now we will explicitly construct such drift orbits for the double dynamical system  $\{\mathcal{F}, \sigma_i\}$ .

Let us partition the domain  $\mathcal{A}$  of the scattering map into three sets:

$$\mathcal{A} = \mathcal{A}_- \cup \mathcal{A}_0 \cup \mathcal{A}_+.$$

$\mathcal{A}_+$  denotes the subdomain where  $\sigma$  gains action,  $\mathcal{A}_-$  where it loses action, and  $\mathcal{A}_0$  where it neither gains nor loses action:

$$\begin{aligned} \mathcal{A}_+ &= \{(I, \phi') \mid I' - I > 0\} = \left\{ (I, \phi') \mid \frac{\partial \tilde{\mathcal{L}}}{\partial \phi'}(I, \phi') > 0 \right\} \\ \mathcal{A}_- &= \{(I, \phi') \mid I' - I < 0\} = \left\{ (I, \phi') \mid \frac{\partial \tilde{\mathcal{L}}}{\partial \phi'}(I, \phi') < 0 \right\} \\ \mathcal{A}_0 &= \{(I, \phi') \mid I' - I = 0\} = \left\{ (I, \phi') \mid \frac{\partial \tilde{\mathcal{L}}}{\partial \phi'}(I, \phi') = 0 \right\}. \end{aligned}$$

These sets are readily identified in Figure 20. For the first scattering map,  $\mathcal{A}_0$  roughly consists of two vertical lines at  $\phi' \approx 0.5$  and  $\phi' \approx 2$ , and  $\mathcal{A}_+$  roughly consists of the vertical strip  $(I, \phi') \in (0, 7] \times (2, 0.5)$ . For the second scattering map,  $\mathcal{A}_0$  roughly consists of two vertical lines at  $\phi' \approx 1.25$  and  $\phi' \approx 3$ , and  $\mathcal{A}_+$  roughly consists of the vertical strip  $(I, \phi') \in (0, 7] \times (3, 1.25)$ .

A simple strategy to produce drift orbits is to *always apply the scattering map if it increases the action* (even if the action gain  $I' - I$  is small). Otherwise, apply the inner map.

This ‘greedy’ algorithm is guaranteed to produce a drift orbit independently of the initial condition, due to the following simple observations: In our model’s domain  $\mathcal{A}$  of validity,

- The inner map  $(I', \phi') = \mathcal{F}(I, \phi)$ , given in Equation (18), is a twist map with frequency  $\nu(I) \approx 6.1$  on the universal cover (see Figure 15), or  $\nu(I) \approx -0.2$  on the base space (where angles are identified modulo  $\pi$ ). Thus the angle  $\phi$  decreases approximately by 0.2 radians at every iterate of the inner map.

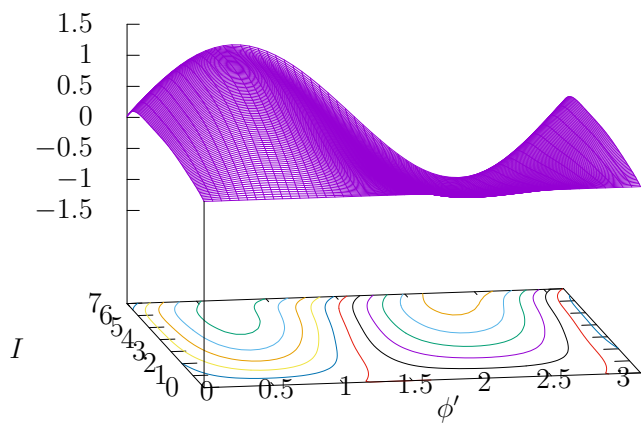
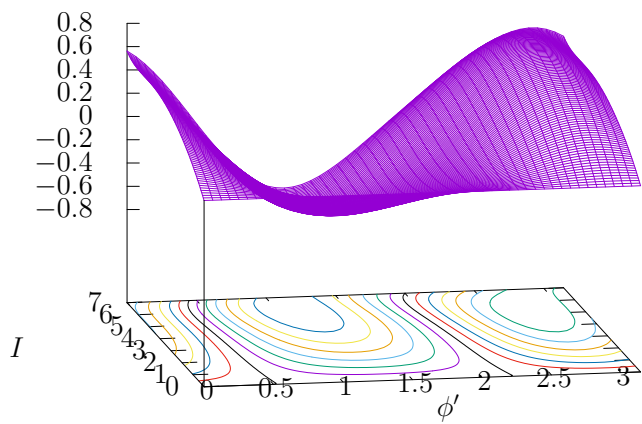


Figure 20: The function  $\frac{\partial \tilde{\mathcal{L}}}{\partial \phi'}(I, \phi')$  for  $\sigma_1$  (above) and  $\sigma_2$  (below). Note that the function  $\phi' \rightarrow \frac{\partial \tilde{\mathcal{L}}}{\partial \phi'}(I_0, \phi')$  attains its maximum at  $\phi' \approx 2.8$  (above) and  $\phi' \approx 0.6$  (below).

- Hence, for any given point  $(I, \phi) \in \mathcal{A}$ , its forward orbit by the inner map eventually enters  $\mathcal{A}_+$ .
- If  $(I, \phi)$  already belongs to  $\mathcal{A}_+$ , we apply the scattering map, increasing the action. Else, we apply the inner map until the orbit enters  $\mathcal{A}_+$ , and then apply the scattering map.

For example, Figure 21 shows the drift orbit produced starting from the initial condition  $(I = 1, \phi = 0)$ . Notice that the drift orbit produced by  $\{\mathcal{F}, \sigma_1\}$  is much longer than the one produced by  $\{\mathcal{F}, \sigma_2\}$ . However, as explained before, these orbits do not directly translate to pseudo-orbits of the RTBP flow, and we don't have control over their drift time.

### 11.2. Triple Dynamical System $\{\mathcal{F}, \tau_1, \tau_2\}$ . Shortest-Time Algorithm.

The algorithms described in previous sections are relatively simple to implement, but they yield sub-optimal pseudo-orbits in terms of their drift time. Now we focus on finding the optimal drift time. This is specially challenging when combining three dynamical systems (inner map, transition map 1, and transition map 2) to construct the pseudo-orbit. Obviously we can't consider all the possible combinations of  $\{\mathcal{F}, \tau_1, \tau_2\}$ , since this number grows exponentially with respect to the length of the orbit. The main idea is to leverage the classic Dijkstra algorithm [50] for finding shortest paths in a graph.

First we partition the domain  $\mathcal{A}$  into a uniform grid of  $m \times n$  two-cells (rectangles) of equal size by dividing  $I \in (0, 7]$  into  $m$  intervals and  $\phi \in [0, \pi)$  into  $n$  intervals. (In practice, we will use  $m = n = 30$ , so the grid consists of 900 small cells).

We introduce a *directed* graph  $G = \langle V, E \rangle$  whose vertices  $V$  represent the different cells. An edge  $e \in E$  from  $u \in V$  to  $v \in V$  means that the center point  $(I, \phi)$  of cell  $u$  is mapped into cell  $v$  either by  $\mathcal{F}$ ,  $\tau_1$ , or  $\tau_2$ . In each case, the edge records the 'distance' between cells, defined as the integration time corresponding to applying  $\mathcal{F}$ ,  $\tau_1$ , resp.  $\tau_2$ .

More precisely, an edge from  $u$  to  $v$  is a pair  $e = (\text{map}, \text{distance})$ , where

- $e = (\mathcal{F}, t_{\text{in}})$  if  $(I, \phi)$  is mapped into  $v$  by the inner map;
- $e = (\tau_1, t_{\text{out}})$  if  $(I, \phi)$  is mapped into  $v$  by the first transition map;
- $e = (\tau_2, t_{\text{out}})$  if  $(I, \phi)$  is mapped into  $v$  by the second transition map;

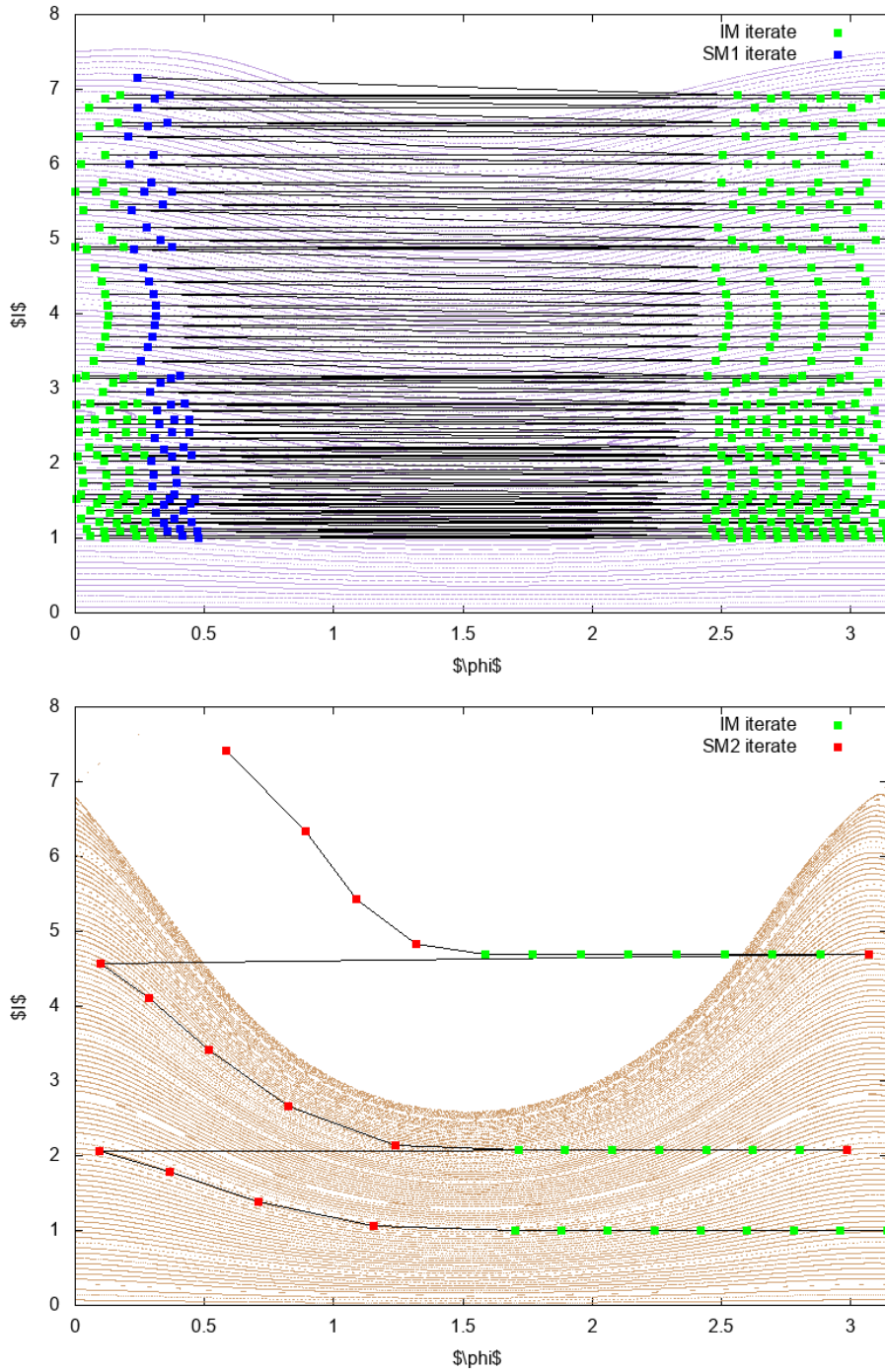


Figure 21: Drift orbit of  $\{\mathcal{F}, \sigma_1\}$  (top panel) and  $\{\mathcal{F}, \sigma_2\}$  (bottom panel) using the greedy algorithm. Green points correspond to iterates of the inner map; blue (resp. red) points correspond to iterates of the first (resp. second) scattering map. Iterates have been joined by line segments to make the orbit more visible. For reference, the orbit is shown against a background consisting of the phase space of the scattering map.

- $e = (\emptyset, \infty)$  if  $(I, \phi)$  is not mapped into  $v$  by neither map.

On rare occasions,  $\tau_1$  and/or  $\tau_2$  can map the center point  $(I, \phi)$  to the same cell as the inner map. If this happens, the inner map is preferred since it takes shorter time, so we set the edge to  $(\mathcal{F}, t_{\text{in}})$ .

*Remark 18.* The image  $(I', \phi')$  of  $(I, \phi)$  by the transition map may be outside  $\mathcal{A}$ . However, this can only happen when  $I' > 7$  (by construction,  $I' < 0$  can never happen). In this case, we associate  $u$  with the closest cell  $v$  to the point  $(I', \phi')$ , namely the cell containing  $(7, \phi')$ .

Given a source cell  $s$  and a destination cell  $t$ , Dijkstra's algorithm applied to  $G$  provides the **shortest (directed) path in the graph** from  $s$  to  $t$  in terms of the distance defined above.

Notice that this path does not exactly correspond to an orbit of the IFS, since we have only considered iterates of center points to construct  $G$  (and the orbit does not necessarily pass through center points, but rather through arbitrary cell points). However, this path clearly *informs* the choice of map  $\{\mathcal{F}, \tau_1, \tau_2\}$  that we should apply when the orbit passes through a given cell.

For example, suppose that the current iterate is inside cell  $u$ , and the shortest path from  $u$  to  $t$  starts with, say,

$$u \xrightarrow{(\tau_1, t_{\text{out}})} v \longrightarrow \dots \longrightarrow t.$$

Then, the best choice given the available information is to apply the first transition map to the current iterate.

Our algorithm to construct optimal orbits (shortest drift time) is given next.

Figure 22 shows the shortest-time orbit from  $x = (I, \phi) = (1, 1.5)$  to a neighborhood of  $y = (I, \phi) = (7, 1.5)$ . The corresponding pseudo-orbit for the RTBP flow takes time  $34t_{\text{in}} + 17t_{\text{out}} \approx 204$  RTBP time units, i.e. about 32 years (optimal drift time). Compare this to the orbits obtained in previous sections.

Notice that the optimal orbit uses all three dynamics  $(\mathcal{F}, \tau_1$  and  $\tau_2)$  for maximum flexibility.

Notice that some iterates actually *decrease* the action. The key point is that, sometimes, one needs to take an iterate that decreases action in order to quickly move to a region where it later increases sharply. This way the pseudo-orbit's time is globally optimized.

---

**Algorithm 1** Shortest-Time Algorithm

---

```
1: procedure ORBITSHORTESTTIME( $x, y$ )    ▷ Shortest-time orbit from
   point  $x \in \mathcal{A}$  to (a neighborhood of) point  $y \in \mathcal{A}$ 
2:    $t \leftarrow cell(y)$                 ▷ Destination cell
3:    $orbit \leftarrow x$                   ▷ Initialize orbit with  $x$ 
4:   while  $x \notin neighborhood(y)$  do    ▷ End when close enough to  $y$ 
5:      $u \leftarrow cell(x)$               ▷ Update current cell
6:      $path \leftarrow Dijkstra(u, t)$      ▷ Shortest path from  $u$  to  $t$ 
7:     if  $path$  starts with  $\mathcal{F}$  then
8:        $x \leftarrow \mathcal{F}(x)$ 
9:     else if  $path$  starts with  $\tau_1$  then
10:       $x \leftarrow \tau_1(x)$ 
11:     else                                ▷  $path$  starts with  $\tau_2$ 
12:       $x \leftarrow \tau_2(x)$ 
13:     end if
14:      $orbit \leftarrow concat(orbit, x)$     ▷ Add iterate  $x$  to orbit
15:   end while
16:   return  $orbit$ 
17: end procedure
```

---



Finally, from the orbit of the IFS  $\{\mathcal{F}, \tau_1, \tau_2\}$  we can construct a pseudo-trajectory by concatenating segments of trajectories of the RTBP flow. Each iterate of the inner map  $\mathcal{F}$  corresponds to its flow suspension, which is integrated using the normal form. Each iterate of the transition map  $\tau_1$  or  $\tau_2$  corresponds to a finite piece of homoclinic trajectory, which is computed by continuation of those previously found in Section 3.

Figure 23 illustrates the construction of the pseudo-trajectory corresponding to the orbit in Figure 22: First,  $\tau_1$  is applied once; this corresponds to the blue homoclinic segment. Then,  $\mathcal{F}$  is applied three times; this corresponds to the green segment. Next,  $\tau_2$  is applied once; this corresponds to the red homoclinic segment. Notice that all segments start and end on the Poincaré section  $\Sigma$  (endpoints are marked with squares). This construction would continue until the whole pseudo-trajectory is obtained (not displayed).

It is important to remark that we obtain a pseudo-trajectory, not a true trajectory of the RTBP. In other words, endpoints of consecutive segments do not exactly match in positions nor velocities, but the discontinuities are small (as it is apparent in Figure 23).

Of course, from this pseudo-trajectory one could find the true RTBP trajectory that shadows it. For applications, however, obtaining the pseudo-trajectory is often the crucial step, since it is ultimately refined in a much more realistic model than the RTBP, e.g. using JPL’s Ephemeris.

## Acknowledgement

AD and PR supported by Spanish grant PID2021-123968NB-I00 (MICIU/AEI/10.13039/501100011033/FEDER/UE). Research of M.G. was partially supported by NSF grant DMS-2307718.

## References

- [1] M. J. Capiński, M. Gidea, Arnold diffusion, quantitative estimates, and stochastic behavior in the three-body problem, *Communications on Pure and Applied Mathematics* 76 (3) (2023) 616–681.
- [2] M. Guardia, V. Kaloshin, P. Martin, P. Roldan, Stochastic behavior along mean motion resonances in the restricted planar three body problem.

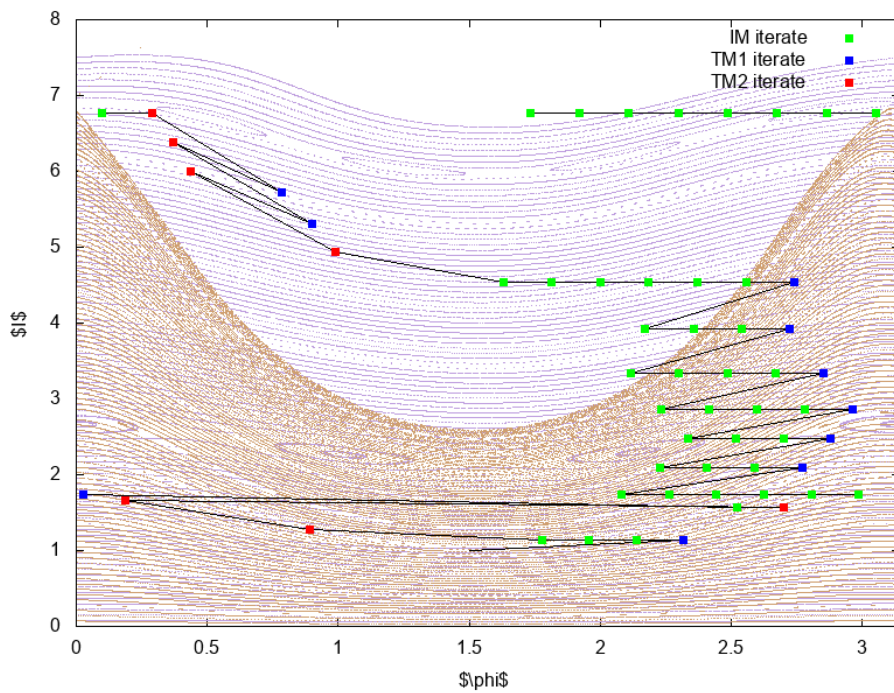


Figure 22: Drift orbit of the triple system  $\{\mathcal{F}, \tau_1, \tau_2\}$  using the shortest path algorithm. Notice that some iterates of the transition map actually *reduce* the action, in order to increase it more efficiently overall.

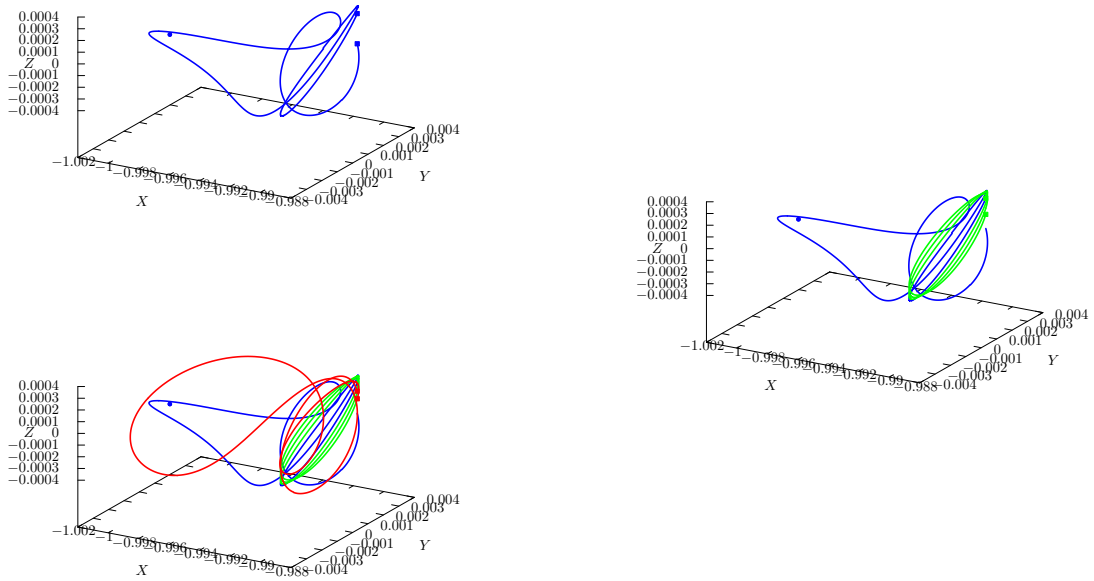


Figure 23: Top left: Trajectory segment corresponding to the first application of  $\tau_1$  in Figure 22 (endpoints are marked with squares). The Earth is represented by a blue circle (not to scale). Middle right: Segments corresponding to  $\tau_1 \circ \mathcal{F}^3$ . Bottom left: Segments corresponding to  $\tau_1 \circ \mathcal{F}^3 \circ \tau_2$ .

- [3] A. Delshams, R. de la Llave, T. M. Seara, A geometric approach to the existence of orbits with unbounded energy in generic periodic perturbations by a potential of generic geodesic flows of  $\mathbf{T}^2$ , *Comm. Math. Phys.* 209 (2) (2000) 353–392.
- [4] A. Delshams, R. De la Llave, T. M. Seara, A Geometric Mechanism for Diffusion in Hamiltonian Systems Overcoming the Large Gap Problem: Heuristics and Rigorous Verification on a Model, Vol. 179, American Mathematical Soc., 2006.
- [5] A. Delshams, R. de la Llave, T. M. Seara, Orbits of unbounded energy in quasi-periodic perturbations of geodesic flows, *Advances in Mathematics* 202 (1) (2006) 64–188.
- [6] A. Delshams, R. de la Llave, T. M. Seara, Geometric properties of the scattering map of a normally hyperbolic invariant manifold, *Adv. Math.* 217 (3) (2008) 1096–1153. doi:10.1016/j.aim.2007.08.014.  
URL <https://doi.org/10.1016/j.aim.2007.08.014>
- [7] A. Delshams, M. Gidea, P. Roldán, Transition map and shadowing lemma for normally hyperbolic invariant manifolds, *Discrete and Continuous Dynamical Systems* 33 (3) (2012) 1089–1112.
- [8] E. Canalias, A. Delshams, J. Masdemont, P. Roldán, The scattering map in the planar restricted three body problem, *Celestial Mechanics and Dynamical Astronomy* 95 (1-4) (2006) 155–171.
- [9] A. Delshams, M. Gidea, P. Roldan, Arnold’s mechanism of diffusion in the spatial circular restricted three-body problem: a semi-analytical argument, *Phys. D* 334 (2016) 29–48. doi:10.1016/j.physd.2016.06.005.  
URL <https://doi.org/10.1016/j.physd.2016.06.005>
- [10] A. Delshams, R. G. Schaefer, Arnold diffusion for a complete family of perturbations, *Regular and Chaotic Dynamics* 22 (2017) 78–108.
- [11] A. Delshams, R. G. Schaefer, Arnold diffusion for a complete family of perturbations with two independent harmonics, *Discrete Contin. Dyn. Syst.* 38 (12) (2018) 6047–6072. doi:10.3934/dcds.2018261.  
URL <https://doi.org/10.3934/dcds.2018261>

- [12] A. Delshams, J. Masdemont, P. Roldán, Computing the scattering map in the spatial Hill's problem, *Discrete Contin. Dyn. Syst. Ser. B* 10 (2-3) (2008) 455–483. doi:10.3934/dcdsb.2008.10.455.  
URL <https://doi.org/10.3934/dcdsb.2008.10.455>
- [13] V. Arnold, Instability of dynamical systems with several degrees of freedom, *Sov. Math. Doklady* 5 (1964) 581–585.
- [14] L. Chierchia, G. Gallavotti, Drift and diffusion in phase space, *Ann. Inst. H. Poincaré Phys. Théor.* 60 (1) (1994) 144.
- [15] S. Bolotin, D. Treschev, Unbounded growth of energy in nonautonomous Hamiltonian systems, *Nonlinearity* 12 (2) (1999) 365.
- [16] D. Treschev, Evolution of slow variables in near-integrable Hamiltonian systems, in: *Progress in nonlinear science, Vol. 1* (Nizhny Novgorod, 2001), RAS, Inst. Appl. Phys., Nizhny Novgorod, 2002, pp. 166–169.
- [17] J. N. Mather, Arnol'd diffusion. I. Announcement of results, *J. Math. Sci. (N. Y.)* 124 (5) (2004) 5275–5289.
- [18] D. Treschev, Evolution of slow variables in a priori unstable Hamiltonian systems, *Nonlinearity* 17 (5) (2004) 1803–1841.
- [19] G. N. Piftankin, Diffusion speed in the Mather problem, *Dokl. Akad. Nauk* 408 (6) (2006) 736–737.
- [20] V. Gelfreich, D. Turaev, Unbounded energy growth in Hamiltonian systems with a slowly varying parameter, *Comm. Math. Phys.* 283 (3) (2008) 769–794. doi:10.1007/s00220-008-0518-1.  
URL <http://dx.doi.org/10.1007/s00220-008-0518-1>
- [21] A. Delshams, G. Hugué, Geography of resonances and Arnold diffusion in a priori unstable Hamiltonian systems, *Nonlinearity* 22 (8) (2009) 1997.
- [22] C.-Q. Cheng, J. Yan, Arnold diffusion in Hamiltonian systems: a priori unstable case, *J. Differential Geom.* 82 (2) (2009) 229–277.  
URL <http://projecteuclid.org/euclid.jdg/1246888485>

- [23] J. N. Mather, Arnold diffusion by variational methods, in: Essays in mathematics and its applications, Springer, Heidelberg, 2012, pp. 271–285. doi:10.1007/978-3-642-28821-0\_11.  
URL [http://dx.doi.org/10.1007/978-3-642-28821-0\\_11](http://dx.doi.org/10.1007/978-3-642-28821-0_11)
- [24] V. Kaloshin, K. Zhang, Arnold diffusion for smooth convex systems of two and a half degrees of freedom, Nonlinearity 28 (8) (2015) 2699–2720. doi:10.1088/0951-7715/28/8/2699.  
URL <https://doi.org/10.1088/0951-7715/28/8/2699>
- [25] P. Bernard, V. Kaloshin, K. Zhang, Arnold diffusion in arbitrary degrees of freedom and normally hyperbolic invariant cylinders, Acta Mathematica 217 (1) (2016) 1–79.
- [26] C.-Q. Cheng, J. Xue, Variational approach to Arnold diffusion, Science China Mathematics 62 (11) (2019) 2103–2130.
- [27] D. Treschev, Arnold diffusion far from strong resonances in multidimensional *a priori* unstable Hamiltonian systems, Nonlinearity 25 (9) (2012) 2717–2757. doi:10.1088/0951-7715/25/9/2717.  
URL <http://dx.doi.org/10.1088/0951-7715/25/9/2717>
- [28] M. Gidea, R. de la Llave, Perturbations of geodesic flows by recurrent dynamics, J. Eur. Math. Soc. (JEMS) 19 (3) (2017) 905–956. doi:10.4171/JEMS/683.  
URL <http://dx.doi.org/10.4171/JEMS/683>
- [29] V. Gelfreich, D. Turaev, Arnold diffusion in a priori chaotic symplectic maps, Communications in Mathematical Physics 353 (2) (2017) 507–547. doi:10.1007/s00220-017-2867-0.  
URL <https://doi.org/10.1007/s00220-017-2867-0>
- [30] M. Gidea, J.-P. Marco, Diffusing orbits along chains of cylinders, Discrete and Continuous Dynamical Systems 0 (2022). doi:10.3934/dcds.2022121.
- [31] V. Kaloshin, K. Zhang, Arnold Diffusion for Smooth Systems of Two and a Half Degrees of Freedom:(AMS-208), Princeton University Press, 2020.

- [32] A. Delshams, V. Kaloshin, A. de la Rosa, T. M. Seara, Global instability in the restricted planar elliptic three body problem, *Communications in Mathematical Physics* 366 (3) (2019) 1173–1228.
- [33] M. Guardia, J. Paradela, T. M. Seara, A degenerate Arnold diffusion mechanism in the restricted 3 body problem, *arXiv preprint arXiv:2302.06973* (2023).
- [34] A. Clarke, J. Fejoz, M. Guardia, Why are inner planets not inclined?, *arXiv preprint arXiv:2210.11311* (2022).
- [35] M. J. Capiński, M. Gidea, R. de la Llave, Arnold diffusion in the planar elliptic restricted three-body problem: mechanism and numerical verification, *Nonlinearity* 30 (1) (2016) 329.
- [36] J.-L. Figueras, A. Haro, Sun-jupiter-saturn system may exist: A verified computation of quasiperiodic solutions for the planar three body problem, preprint at [arxiv.org/abs/2403.10152](https://arxiv.org/abs/2403.10152), submitted March 2024.
- [37] E. Belbruno, *Capture Dynamics and Chaotic Motions in Celestial Mechanics: With Applications to the Construction of Low Energy Transfers*, Princeton University Press, 2004.
- [38] M. Barcelona, A. Haro, J.-M. Mondelo, Semianalytical computation of heteroclinic connections between center manifolds with the parameterization method, *SIAM J. Appl. Dyn. Syst.* 23 (1) (2024) 98–126. doi:10.1137/23M1547883.  
URL <https://doi.org/10.1137/23M1547883>
- [39] V. Szebehely, *Theory of Orbits*, Academic Press, 1967.
- [40] A. Jorba, J. Masdemont, Dynamics in the center manifold of the collinear points of the restricted three body problem, *Phys. D* 132 (1-2) (1999) 189–213. doi:10.1016/S0167-2789(99)00042-1.  
URL [https://doi.org/10.1016/S0167-2789\(99\)00042-1](https://doi.org/10.1016/S0167-2789(99)00042-1)
- [41] A. Jorba, A methodology for the numerical computation of normal forms, centre manifolds and first integrals of Hamiltonian systems, *Experiment. Math.* 8 (2) (1999) 155–195.  
URL <http://projecteuclid.org/euclid.em/1047477059>

- [42] A. Delshams, P. Gutiérrez, Estimates on invariant tori near an elliptic equilibrium point of a Hamiltonian system, *J. Differential Equations* 131 (2) (1996) 277–303. doi:10.1006/jdeq.1996.0165.  
URL <https://doi.org/10.1006/jdeq.1996.0165>
- [43] M. J. Capiński, P. Roldán, Existence of a center manifold in a practical domain around  $L_1$  in the restricted three-body problem, *SIAM J. Appl. Dyn. Syst.* 11 (1) (2012) 285–318. doi:10.1137/100810381.  
URL <https://doi.org/10.1137/100810381>
- [44] J. Milnor, Morse theory, Vol. No. 51 of *Annals of Mathematics Studies*, Princeton University Press, Princeton, NJ, 1963, based on lecture notes by M. Spivak and R. Wells.
- [45] V. I. Arnold, A. Avez, Ergodic problems of classical mechanics, W. A. Benjamin, Inc., New York-Amsterdam, 1968, translated from the French by A. Avez.
- [46] A. Haro, An algorithm to generate canonical transformations: application to normal forms, *Phys. D* 167 (3-4) (2002) 197–217. doi:10.1016/S0167-2789(02)00459-1.  
URL [https://doi.org/10.1016/S0167-2789\(02\)00459-1](https://doi.org/10.1016/S0167-2789(02)00459-1)
- [47] R. Moeckel, Generic drift on Cantor sets of annuli, in: *Celestial mechanics* (Evanston, IL, 1999), Vol. 292 of *Contemp. Math.*, Amer. Math. Soc., Providence, RI, 2002, pp. 163–171. doi:10.1090/conm/292/04922.  
URL <https://doi.org/10.1090/conm/292/04922>
- [48] P. Le Calvez, Drift orbits for families of twist maps of the annulus, *Ergodic Theory and Dynamical Systems* 27 (3) (2007) 869–879.
- [49] M. Gidea, R. de la Llave, T. M-Seara, A general mechanism of diffusion in Hamiltonian systems: Qualitative results, *Communications on Pure and Applied Mathematics* 73 (1) (2020) 150–209.
- [50] E. W. Dijkstra, A note on two problems in connexion with graphs, *Numer. Math.* 1 (1959) 269–271. doi:10.1007/BF01386390.  
URL <https://doi.org/10.1007/BF01386390>